Spring 2023

Development and Testing of a Hyperbaric Aerodynamic Levitator for Containerless Materials Research

Sydney Elizabeth Boland
Missouri University of Science and Technology

Department:

DEVELOPMENT AND TESTING OF A HYPERBARIC AERODYNAMIC LEVITATOR FOR CONTAINERLESS MATERIALS RESEARCH

by

SYDNEY ELIZABETH BOLAND

A THESIS

Presented to the Graduate Faculty of the

MISSOURI UNIVERSITY OF SCIENCE AND TECHNOLOGY

In Partial Fulfillment of the Requirements for the Degree

MASTER OF SCIENCE IN MATERIALS SCIENCE AND ENGINEERING

2023

Approved by:

Dr. David Lipke, Advisor
Dr. Joseph Newkirk
Dr. Jeremy Watts

PUBLICATION THESIS OPTION

This thesis consists of the following three articles, formatted in the style used by the Missouri University of Science and Technology:

Paper I, found on pages 22 – 45, has been submitted to *Review of Scientific Instruments*.

Paper II, found on pages 46 – 55, is intended for submission to *Journal of Solid State Chemistry*.

Paper III, found on pages 56 – 64, is intended for submission to *Journal of the American Ceramic Society*.

ABSTRACT

This research focused on the development and testing of a hyperbaric aerodynamic levitator for containerless materials research of specimens at temperatures greater than 2000°C and pressures up to 10.3 MPa (1500 psi). The effect of specimen size, specimen density, pressure, and flow rate on the levitation behavior was studied. Lightweight specimens demonstrated two stable levitation regimes that were speculated to be associated with a change in the turbulent wake structure. The hyperbaric aerodynamic levitator was also used to determine the effect of pressure on the heat transfer by studying the melting behavior of a levitated 3.0 mm diameter alumina sphere melted with a continuous wave CO_2 laser. The convective heat transfer coefficient increased threefold from atmospheric pressure to 10.3 MPa. However, the additional output laser power necessary at 10.3 MPa was only approximately 60 W, demonstrating the feasibility of the system. To demonstrate the benefits of high reactive gas pressure, further melting studies with aluminum oxynitride and chromium nitride were completed. Aluminum oxynitride specimens were melted in N_2 at atmospheric pressure and 10.3 MPa to determine the effect of gas pressure on the phase composition. Preliminary X-ray diffraction results indicated a difference in phases present at atmospheric pressure and 10.3 MPa. A net mass loss of 5.68 wt.% was observed at atmospheric pressure, while at 10.3 MPa, the mass loss was 0.27 wt.%. Similarly, chromium nitride samples were melted in N_2 at atmospheric pressure and 5.52 MPa (800 psi) to determine the effect of gas pressure on the phase composition. A more significant mass loss of 60.22 wt.% was noted at atmospheric pressure compared to the 23.64 wt.% mass loss at 5.52 MPa.

ACKNOWLEDGMENTS

I would like to thank my advisor, Dr. David W. Lipke, for his guidance and assistance throughout my graduate studies. I appreciate the opportunity he provided me to join his research group and further my education. With his guidance, I have been able to experience many wonderful research opportunities, and I have had the opportunity to grow as an engineer. He has always been ready to assist and provide advice, whether that is regarding research or any other general advice. Dr. Lipke and his enthusiasm for this research has made this a rewarding graduate school experience.

Thank you as well to my collaborators on this project: Rick Weber, Stephen Wilke, and Sarah Schlossberg from Materials Development Inc., who provided assistance and the use of their facilities to perform initial melting trials with our hyperbaric aerodynamic levitator as well as studies with aluminum oxynitride and chromium nitride.

Thank you to my peers in the Lipke research group for their help and support. They provided me with assistance in using equipment, and they have been a great source of learning for me. Thank you to them for always being willing to answer my questions and provide a helping hand.

Finally, thank you to my family and friends for all their support throughout the years. I would not be where I am without the support of my family; they have always inspired me and encouraged me to do my best.

TABLE OF CONTENTS

Page

LIST OF ILLUSTRATIONS

SECTION Page

PAPER I

PAPER III

LIST OF TABLES

NOMENCLATURE

Symbol	Description
Fc	Electric Force
q	Charge
E	Electric Field
d	Diameter of Sphere
D	Diameter of Nozzle
ρ_s	Density of Sphere
ρ	Density of Fluid
Z/d	Relative Levitation Height
g	Standard Acceleration due to Gravity
v	Velocity
Q	Volumetric Flow Rate
C_d	Drag Coefficient
A	Momentum Flux Constant
β	Cone Angle of the Nozzle
Fr	Froude Number
h	Convective Heat Transfer Coefficient
c_p	Heat Capacity
ε	Emissivity
σ	Stefan-Boltzmann Constant

1. INTRODUCTION

Containerless processing is a useful tool for materials researchers in studying the behavior of materials at high temperature without the effect of container walls. By avoiding contact with container walls, contamination from chemical interactions with the container can be eliminated. Containerless processing also allows for the elimination of heterogeneous nucleation sites.[1] Avoiding these heterogeneous nucleation sites allows for the deep undercooling of materials and the ability to access novel phases.[1] There are several methods for containerless processing studies, many of which include work with ground-based levitation techniques. Levitators have a history of being used to synthesize and study ultra-high purity semiconductors[2,3] and bulk metallic glasses.[4] Pairing levitators with directed energy sources allows for specimen temperatures greater than 2000°C to be attained for material processing. Additionally, levitators can serve as an environment for *in-situ* characterization including synchronization beamlines for atomic structure data and structural chemistry information.[5-12]

There are four main types of levitation techniques: acoustic, aerodynamic, electromagnetic, and electrostatic, along with combinations of these.[1,13-15] This work concentrates on the development of a special purpose aerodynamic levitator. Aerodynamic levitation operates on the principle of overcoming the gravitational force to levitate a sphere by supplying a gas flow. This condition is derived from a force balance between the gravitational force and momentum transfer from the levitating gas, which is a function of the drag force.[1] Aerodynamic levitation offers the advantage of the ability to

utilize the processing gas to make *in-situ* chemistry changes. Changing the processing gas allows for new redox states of materials to be accessed.

Hyperbaric aerodynamic levitation offers additional advantages over levitation at atmospheric pressure (0.1 MPa). One benefit to an elevated pressure system is the ability to suppress volatilization, which allows samples to be better preserved.[16,17] Specimens can be observed for longer durations at elevated pressures, enabling measurements of properties or structural chemistry of volatile materials. The other main advantage to high pressure systems is that the increase in fugacity leads to the increase in chemical potential, $\Delta\mu_i = RT \ln f_i/f_i^\circ$. With an increase in chemical potential, there is a possibility for unique phase formations that cannot be achieved at atmospheric pressure along with the synthesis of new compounds. This effect has been explored previously with high pressure crystal growth work.[18-26]

Hyperbaric aerodynamic levitation is a promising technique that allows for the study of materials that cannot be processed or studied under atmospheric pressure in a containerless system. Aluminum oxynitride (AlON) is a material of interest to study at elevated N_2 pressures due to the effect of N_2 pressure on the lattice parameter. Increasing the N_2 pressure affects the nitrogen content by suppressing Al_2O vapors, which can lead to shifts in the lattice parameters.[27] AlON is a material of interest due to its combination of mechanical, thermal, and optical properties. It has a greater than 80% transmittance of ultraviolet and mid-infrared light, and it has excellent mechanical properties, such as a high Knoop hardness of 1800 kg/mm^2 and a room temperature flexural strength of 306 MPa.[28]

Similarly, chromium nitride (Cr_2N) is of interest to study, as it will decompose before reaching its melting point at atmospheric pressure. However, if the pressure is increased, melting can be achieved without decomposition and net reduction of nitrogen.[29] Cr_2N is also a useful material to study due to its hot corrosion resistance along with its high hardness and wear resistance.[30-32] Hyperbaric aerodynamic levitation provides an avenue to study these materials without influence from high temperature container interactions.

This work details the design and testing of a hyperbaric aerodynamic levitator for materials containerless processing research. This levitator operates at pressures ranging from atmospheric to 10.3 MPa and temperatures greater than 2000°C when paired with a continuous wave CO_2 (CW CO_2) laser. Levitation behavior was assessed by studying the effect of sample size, sample density, pressure, and flow rate on stable levitation. Furthermore, this system was tested to determine the effect of pressure on the convective heat transfer losses by studying the melt behavior of a levitated molten alumina (Al_2O_3) sample. The convective heat transfer coefficient was calculated at a range of pressures, and the output laser power necessary to reach the melting point was assessed at atmospheric pressure and 10.3 MPa. Additionally, the study of AlON and Cr_2N is detailed to compare the effects of N_2 pressure on phase formation and lattice parameter shifts. AlON and Cr_2N were melted in the hyperbaric aerodynamic levitator at atmospheric pressure and elevated pressure, and samples were recovered to determine the mass change after processing. X-ray diffraction (XRD) was performed to determine differences in phase composition with changing pressure.

2. LITERATURE REVIEW

2.1. CONTAINERLESS PROCESSING

Containerless processing is a technique that eliminates contact between a material and a container during material processing.[33] It is used for the synthesis and study of novel materials at high temperatures under non-equilibrium conditions.[33] Containerless processing offers many advantages including the avoidance of contamination at high temperatures.[12,13,33] With increasing temperature, the possibility of chemical reaction between the container surface and molten material increases, leading to contamination of the sample.[13] Containerless processing offers a route to producing and studying high-purity materials due to the lack of container contamination.

Another advantage to containerless processing is the elimination of heterogeneous nucleation sites. Contact between a molten sample and the container can also lead to extrinsic heterogeneous nucleation, which limits the amount of undercooling that can be achieved.[33] Eliminating heterogeneous nucleation sites allows for melts to be deeply undercooled due to the high nucleation barrier before solidification, which can affect the microstructure of the material.[34] Novel metastable and amorphous phases can be achieved due to this solidification.[34] Deep supercooling is a prerequisite for glass formation; therefore, containerless processing is an attractive solution for the formation and study of novel glasses.[33]

There are several methods for containerless processing which can be characterized as either transient or steady-state containerless processing techniques. Transient techniques utilize the free fall or entrainment of sample particles to achieve

containerless processing.[13] This can include drop-tube methods, where a drop free falls with sufficient times for solidification. Steady-state techniques utilize a sustained directed force to overcome gravity and achieve levitation at a fixed position for a long duration.[1] Steady-state techniques include microgravity experiments as well as ground-based levitation techniques. There are four main ground-based levitation techniques: acoustic levitation, aerodynamic levitation, electrostatic levitation (ESL), and electromagnetic levitation (EML). Other techniques include gas film, magnetic, and hybrid methods, such as aero-acoustic[9] or electrostatic-aerodynamic.[13,14]

Steady-state ground-based levitation techniques are valuable for the synthesis of novel materials, as well as *in-situ* characterization during material processing at high temperatures. Levitators are used in conjunction with directed energy sources, such as CW CO_2 lasers, electron beams, or electromagnetic inductive coupling, to achieve temperatures greater than 2000°C. This allows for capabilities to synthesize materials, study chemistry and atomic structure, and perform thermophysical property measurements. Levitators have previously been used to study solidification and vitrification of materials undergoing solid-liquid phase transitions during processing, allowing for the study and synthesis of novel materials. Materials synthesized using levitation have included ultra-high purity semiconductors[2,3] and bulk metallic glasses.[4]

In addition to the synthesis of novel materials, these systems are useful for the study of materials at high temperatures. Levitation techniques allow for thermophysical measurements of liquids at high temperatures without the influence of container interactions and interference. Thermophysical property measurements of enthalpy of fusion, density, surface tension, viscosity, and thermal conductivity have been completed

on levitated samples.[35-41] Different types of levitator systems are each suited for the measurements of particular properties. For example, electrostatic levitation has been used to measure density by imaging, surface tension, and viscosity of metals. However, aerodynamic levitation is suitable for the measurement of the density of liquids, but the determination of surface tension and viscosity has been more difficult.[33] The enthalpy of oxides at high temperatures has been measured using a system known as a drop-and-catch calorimeter.[42] This works by using a 'split nozzle' design, allowing the nozzle to be separated along a vertical join.[42] The nozzle can open to allow the hot sample to fall into a calorimeter enabling the measurement of the heat content.[42]

These systems can also be integrated with radiation scattering experiments to determine atomic and crystalline structure information via X-ray diffraction, spallation neutron diffraction, and X-ray absorption near edge structure (XANES). The high energy X-ray beams and neutron beams probe the top 100-200 μm of a levitated sample to determine the structure and dynamics of materials.[33] Wide angle high-energy X-ray diffraction has been used with aerodynamic levitation to collect scattering data for the liquid and crystalline state of materials, as well as frequently being used in glass studies.[33]

2.1.1. Acoustic Levitation. Work on acoustic levitation began with Bucks and Muller[43] and was further developed by many others.[44-48] Acoustic levitation uses an acoustic radiation force resulting from an impedance difference between the suspension media and the solid or liquid sample to counteract the force of gravity and levitate a small sample.[49] A gas medium is typically used as the suspension media to propagate the sound waves. Acoustic levitation can be classified into two types: standing wave acoustic

levitation and near-field levitation.[49] The standing wave acoustic levitation is most common, where small solid and liquid materials are suspended in the pressure nodes of a standing wave field. Single-axis acoustic levitators (SAL), a type of standing wave acoustic levitation, consists of a vibrating source and a reflector to improve efficiency.[50] SAL can be used to levitate any sample, including high density materials such as tungsten, often ranging in size from 0.5-3.0mm; however, this system typically operates in a lower temperature range.[33] Many studies with acoustic levitation have been completed in the temperature range of -40°C to 250°C.

2.1.2. Electromagnetic Levitation. Electromagnetic levitation was one of the first containerless processing techniques developed by Muck51 in 1923 for the levitation of metallic samples. The basic operating principle for electromagnetic levitation comes from the force for levitation produced by the induction of eddy currents in a metallic sample by an alternating electromagnetic field.4 The sample is positioned in a potential well generated by electromagnetic fields and is self-stabilizing. Solid samples oscillate about the equilibrium position with a frequency normally in the range of 5 Hz, while liquid samples exhibit free surface oscillations with a frequency usually in the range of 50 Hz.52 The samples for EML must be conductive, typically in the size range of 2-6 mm, and experiments can be performed in gas or high vacuum.

2.1.3. Electrostatic Levitation. Rhim et al. pioneered the development and use of electrostatic levitation.[4] Electrostatic levitation utilizes a vertical electric field to levitate a sample that is charged or polarized. Levitation is achieved through the Coulomb force where q is the charge on the sample.[52]

$$F_C = qE \tag{1}$$

The sample's charge must be maintained throughout the levitation, and due to the high voltages applied, ESL is often done under ultra-high vacuum.[37] ESL is used for thermophysical property measurements, solidification, structural studies, and mechanical properties of metallic materials.[53]

2.1.4. Aerodynamic Levitation. Aerodynamic levitation of solids was initially performed by Winborne et al.,[54] while levitation of molten samples was performed later by Coutures et al. in 1986.[55] This technique utilizes a gas flow to levitate a sample by overcoming the gravitational force. The condition for aerodynamic levitation is derived from the force balance between the gravitational force and the force from the levitating gas, which is a function of the drag coefficient, C_d, fluid density, ρ, flow velocity, v, and pressure drop over the area of the sample, A.[33]

$$Mg = C_d \int (\rho v^2 + p) dA \quad (2)$$

Aerodynamic levitation is usually achieved with use of a converging-diverging nozzle, known as conical nozzle levitation (CNL). There can be many different designs of the conical nozzle as shown in Figure 2.1.[33] The cone typically has a semi-angle of 30-60° and an orifice of 0.5-3 mm.[33] Recent nozzle designs are reduced in size from early nozzle designs,[54] allowing for more of the levitated sample to be visible. Recent designs allow for 30-70% of the sample to levitate above the plane of the nozzle, while early designs were deep and only visible when viewed from above.[8,33,54,56] The material used to produce these nozzles include aluminum alloy, stainless steel, vanadium, as well as nonmetallic materials, such as boron nitride, graphite, and machinable ceramic.[33] Aluminum alloy is a popular choice of material due to its durability and ability to be easily cleaned.[33]

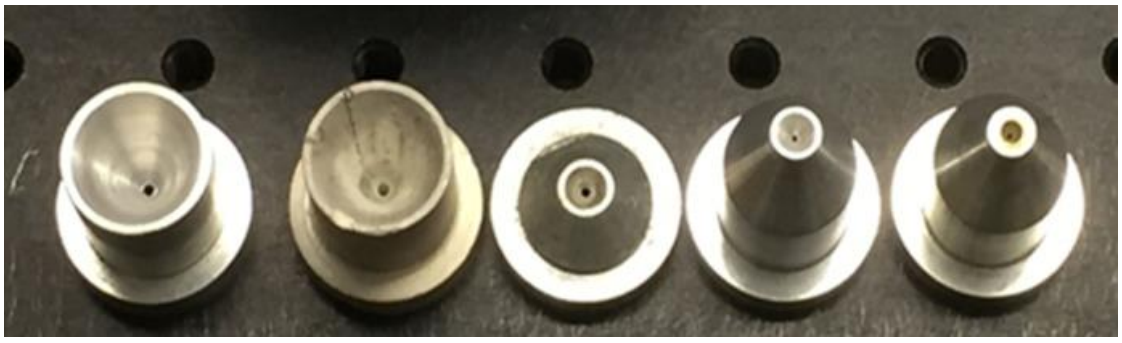

Figure 2.1: Examples of differing nozzle designs beginning with early deep nozzles on the left and moving to designs towards the right that allow for the levitated sample to be viewed along the horizontal direction. Adapted from C.J. Benmore and J.K.R. Weber.[33]

Aerodynamic levitation has been utilized to levitate spherical specimens ranging in diameter from 2.0-4.0 mm.[14,57-65] The material choice for aerodynamic levitation is not limited to electrically conductive specimens, as is the case for EML, providing the opportunity for the processing and studying of metals, semiconductors, and ceramic oxides.[66] The gaseous environment required to provide the levitation force allows for the use of the gas to adjust the chemistry of a specimen *in-situ*. This gas can be purified to part per billion (ppb) levels, avoiding the need for ultrahigh vacuum systems when processing metallic samples prone to oxidation.

One study completed by C. Shi et al. took advantage of the gaseous environment for aerodynamic levitation and investigated the structures of stable and supercooled iron oxide melts as a function of oxygen fugacity and temperature.[67] The oxygen partial pressure was controlled using different gas mixtures for levitation, and *in-situ* XRD was able to provide structural information for the iron oxide melts.

While aerodynamic levitation offers many advantages, a disadvantage of the technique is the temperature gradients that arise from laser heating with aerodynamic levitation. A study completed by McCormack et al. investigated the thermal gradients on

specimens levitated in a CNL and melted with a CW CO_2 laser.[68] The study completed by McCormack et al. showed that thermal gradients can be minimized by maximizing the sphericity of the specimen and the density along with minimizing microstructural features.[68] These properties allow for rotation of the specimen around multiple axes, leading to homogeneous heating and reduced thermal gradients. Figure 2.2 shows the temperature difference monitored from two points on the specimens.[68] As shown here, the commercially provided specimens that were perfectly spherical and dense (ZrO_2 and ruby) showed a much lower thermal gradient.

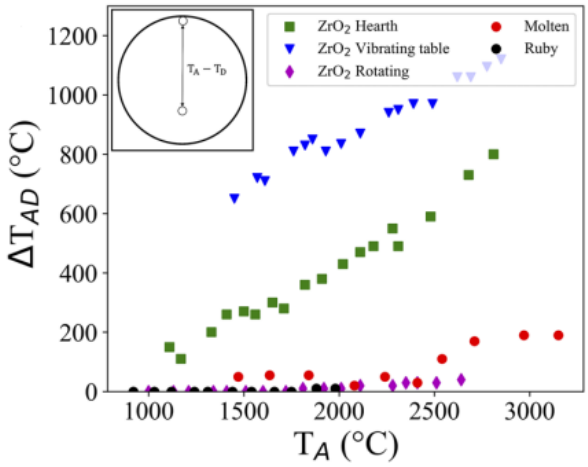

Figure 2.2: Thermal gradients at varying temperatures between points T_A and T_D (indicated on the image) for materials prepared via different processing routes. Adapted from McCormack et al.[68]

The specimens for this study were prepared via different routes to determine the effect of processing on the temperature gradient. As samples are required to be spherical for aerodynamic levitation, there are multiple processing routes to attain this shape. Typically, samples, such as ceramic oxide spheres, are formed using the molten hearth

method.[69] In this method, powder is heated in a copper-hearth with a sealed tube CO_2 laser, and due to the strong surface tension of an oxide liquid, spheroids are formed. However, a drawback with this method is the inability to control composition and phases as some materials may be volatile above their melting point, and metastable phases can form upon quenching from a melt. Another method to produce spherical samples is the "vibrating table" method.[70-72] In this method, a ceramic slurry is prepared and vibrated at a frequency of around 70 Hz in a cubed-wall container. This method can produce spheroids due to the presence of a shear thinning binder. The spheroids can then be calcined and sintered at low temperatures. However, these low temperatures result in low density specimens. Perfectly spherical materials can also be provided commercially and manufactured with the Verneuil process or via a ball milling process.

2.2. EFFECT OF HIGH PRESSURE

While levitation at ambient pressures for the study and synthesis of materials has been studied for decades, there are fewer examples of levitators capable of performing under hyperbaric conditions. High pressure, however, provides benefits that cannot be achieved with levitation work at atmospheric pressures. One such benefit is the suppression of volatile losses. As the vapor pressure increases with increasing temperature, evaporation of the sample can be observed. By suppressing volatilization, sample chamber windows used for sample viewing, pyrometry access, and laser access will be less susceptible to deposition from the melting sample. Additionally, by suppressing volatilization, the composition is better preserved, allowing for a more consistent sample chemistry.[73] This

also allows for *in-situ* property measurements due to the extended life of the specimen itself at high temperatures.

Another benefit to containerless processing under hyperbaric operating conditions is the increase in fugacity with a reactive gas species, such as oxygen or nitrogen. Increases in the fugacity, f_i, leads to increases in the chemical potential, $\Delta\mu_i = RT \ln f_i/f_i^\circ$, which can affect the phase equilibria of a sample. As shown with this relationship, both temperature and fugacity are important for increasing the chemical potential. Temperature has a large effect on the chemical potential as there is a linear relationship, while fugacity affects the chemical potential on a logarithmic scale. Within the pressure range of P = 10 – 10,000 bar, inert and reactive gases transition to liquids or supercritical fluids.[74] Changes in fluid pressure result in order of magnitude changes in chemical potential.[74]

An example of this principle is the La-Ni-O system.[75] At 1 bar (0.1 MPa) of O_2 gas pressure, La_2NiO_4 is the most stable ternary at higher temperatures above T_1, as it has the lowest energy as shown in Figure 2.3.[74,75] The higher valence La-Ni-O ternaries that are formed are from a reaction of La_2NiO_4 and oxygen. These reactions have a negative net entropic change, meaning that the formation of these higher valence states becomes unfavorable at higher temperatures. However, with increasing oxygen pressure (denoted by the blue lines in Figure 2.3), the equilibrium is shifted towards the valent species, and between the range of T_1 and T_2, $LaNiO_3$ has the lowest energy and becomes the most stable state.[74,75] This example shows that changing the pressure of reactive gases affects the chemical potential and phase stabilities.

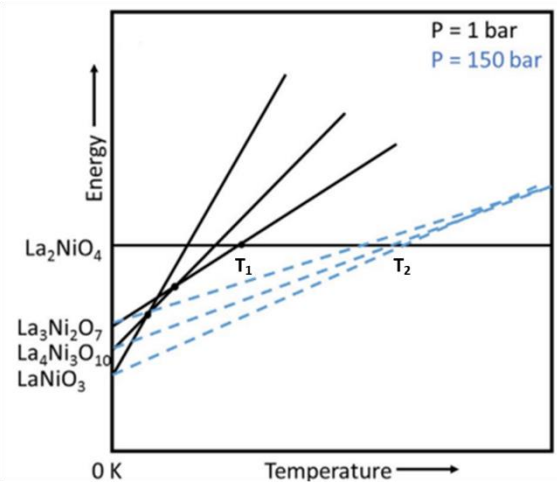

Figure 2.3: La-Ni-O system demonstrating the effect of pressure changes of reactive gases on the chemical potential and phase stability. Adapted from W.A. Phelan et al.[74]

High-pressure crystal growth is one such example taking advantage of the increased fugacity.[74] High pressure floating zone furnaces have been designed as shown in Figure 2.4 for crystal growth.[76] There have been many studies that have crystallized materials by high pressure optical zone growth at pressures greater than 30 bar (3MPa).[75,77-84]

There have been examples of special use levitators as well that have been operated at elevated pressures. For example, there have been multiple examples of high-pressure acoustic levitators.[85-88] One such example of an acoustic levitator used at elevated pressures is the study of mass transport processes on suspended samples.[86] This work was completed at operating temperatures up to 180°C and pressures of 30 MPa.[86] Other work has been completed with hybrid aerodynamic-electrostatic levitation,[9] electrostatic levitation,[89] and electromagnetic levitation.[90,91] The hybrid aerodynamic-electrostatic levitator proved the feasibility of levitating and melting oxide material samples in a pressurized environment to 1 MPa.[9] The electrostatic levitator was

pressurized to 0.4 MPa and operated at temperatures ranging from 400-2000°C to measure the density of calcium aluminate in gas atmospheres of oxygen, nitrogen, and air.[89] An example of electromagnetic levitation at elevated pressures has been studied to understand the kinetics of gas-liquid metal reactions with levitated drops.[90] The decarburization of the levitated molten iron-carbon alloys was studied in gas mixtures at temperatures of 1650°C and pressures of 4 MPa.[90]

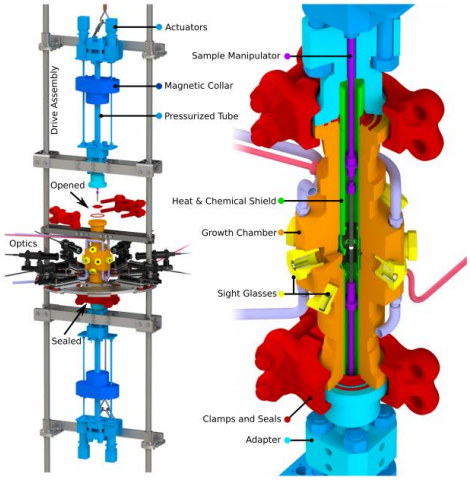

Figure 2.4: Schematic of overall assembly for high pressure floating zone crystal growth (left) with exploded view of the core components (right). Adapted from J.L. Schmehr et al.[76]

2.3. MATERIALS OF INTEREST AT HIGH PRESSURE

As stated previously, there are many advantages to increased pressure in the synthesis and study of materials. Elevated pressure can allow for the access of new phase states and prevent the decomposition of phases at elevated temperatures. Nitrides, specifically, provide many materials of interest to study with a reactive gas at elevated pressures. One such material is aluminum oxynitride due to the shift in lattice parameters

that is observed with changing N_2 pressure. Chromium nitride is also a material of interest due to the decomposition that occurs at atmospheric pressure prior to reaching the melting point. However, at an increased pressure, this melting point can be accessed, allowing for the preservation of the phases present.

2.3.1. Aluminum Oxynitride. Aluminum oxynitride materials can be transparent ceramics depending on the microstructure and relative density. AlON has been produced with a grain size ranging from 150-200 μm and a relative density greater than 95% to attain optical transparency.[92] This is utilized frequently in defense applications for transparent armor for helicopters, aircraft, and ground vehicles, along with domes for IR guided missile systems and IR sensors for reconnaissance pods.[28] AlON has many properties that make this material ideal for these applications, including its transparency, allowing it to act as a window material due to the greater than 80% transmission in the wavelength range from ultraviolet to mid-infrared light.[28] Other basic properties of AlON provided by McCauley and Corbin are summarized in Table 2.1.[93] This sample was pressureless sintered into a nearly pore free, single-phase material.

Table 2.1: Summary of AlON properties of a pressureless sintered sample recorded by McCauley and Corbin.[93]

Property	**Value**
Knoop Hardness	1800 kg/mm^2
Elastic Modulus	3.3 x 10^5 MPa
Room Temperature Strength	306 MPa
High Temperature Strength (1000°C)	267 MPa
Thermal Expansion (α) from RT-1000°C	7 x 10^{-6}/°C

AlON is a cubic spinel phase in the Al_2O_3-AlN system that was first reported by Yamaguchi and Yanagida in 1959.[94] Since that time, this result has been confirmed, and additional phase diagrams have been constructed. McCauley and Corbin completed the work to create the full Al_2O_3-AlN pseudo-binary phase diagram including the AlON phase as shown in Figure 2.5.[93] Their diagram shows the composition centered on 35.7 mol% AlN, and a melting temperature of AlON at 2165°C in 1 atm (0.1 MPa) of flowing N_2 gas.

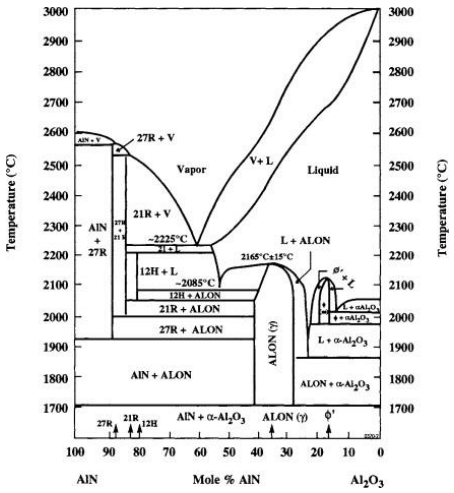

Figure 2.5: Phase diagram of the pseudo-binary Al_2O_3-AlN system in 0.1 MPa of flowing N_2 gas. Adapted from McCauley and Corbin.[93]

AlON has been synthesized by many different routes, including the reaction sintering of Al_2O_3 and AlN,[95-97] carbothermal reduction of Al_2O_3,[98] plasma arc synthesis,[99,100] and self-propagating high-temperature synthesis (SHS).[101] For reaction sintering of Al_2O_3 and AlN to form AlON, powder mixtures of Al_2O_3 and AlN are sintered at temperatures greater than 1650°C in a flowing N_2 atmosphere for the formation of single phase AlON.[95-97] Often these reactions occur with additives, such as

Y_2O_3, to aid in sintering and increasing the densification.[95-97] For the carbothermal reduction of Al_2O_3, Al_2O_3 is mixed with carbon in varying ratios and milled together before being reacted at temperatures near 1700°C in flowing N_2.[98] In plasma arc synthesis, Al_2O_3 and AlN powders are milled and pressed into pellets before being placed in a DC arc-melting furnace.[99,100] A high purity gas is introduced into the chamber and the samples are quickly melted in the plasma. To synthesize AlON via SHS, the combustion of aluminum metal and Al_2O_3 is performed in a flowing N_2 atmosphere.[101] Following this, samples are manufactured by grinding the powder and hot-pressing or spark plasma sintering billets.

AlON is of interest to study at elevated pressures because the structure has a strong dependence on the pressure of N_2 gas as observed by shifts in the lattice parameter. The change in lattice parameter is dependent on temperature, pressure, and nitrogen content. One study investigated the effect of N_2 pressure on the combustion synthesis of AlON and measured the nitrogen content and lattice parameter as a function of N_2 pressure.[102] These combustion reactions were completed at pressures ranging from 10-60 MPa and the combustion temperature was approximately 1850°C. As shown in Figure 2.6, the nitrogen content and lattice parameter increased with increasing nitrogen pressure.[102] McCauley et al. similarly reported that in the temperature range of 1800-1950°C, the lattice parameter increased linearly with nitrogen content.[27] However, McCauley et al. reported that this relationship changed with further increasing temperature.

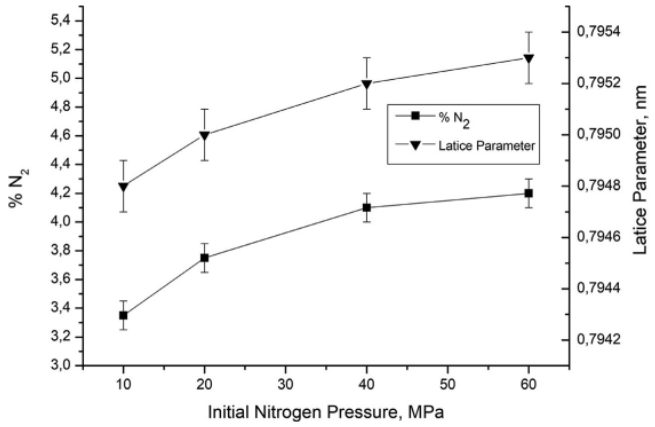

Figure 2.6: Lattice parameter and nitrogen content dependence on N_2 pressure for the combustion synthesis of AlON. Adapted from T.G. Akopdzhanyan et al.[102]

McCauley et al. further reported work that was performed at temperatures greater than 2000°C and also demonstrated the dependence of low N_2 pressures on the lattice parameter. [27] Figure 2.7 illustrates this phenomenon of N_2 pressure dependence.[27] This work shows a decreasing lattice parameter with increasing nitrogen pressure. The lattice parameter is a reflection of the change in ratio of nitrogen content to oxygen content. The lattice parameter, therefore, is dependent on the nitrogen content. As the N_2 pressure increases, the nitrogen content is reduced due to the suppression of the Al_2O vapor phase, meaning there is more relative oxygen.[103] The loss of nitrogen content, or the composition shift towards Al_2O_3, is associated with a reduced lattice parameter as shown in Figure 2.7.[27] When comparing the two studies, it can be noted that there is a temperature dependence on the relationship between lattice parameter and N_2 pressure, impacting the trend observed.

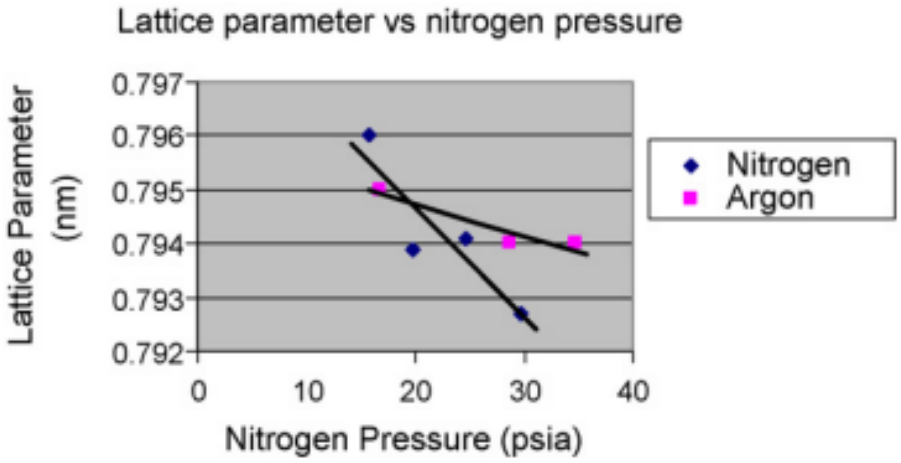

Figure 2.7: Lattice parameter vs. nitrogen and argon pressure for a AlON specimen heated at 2000°C for 30 minutes. Adapted from J.W. McCauley et al.[27]

2.3.2. Chromium Nitride. Chromium nitrides are frequently used as thin film coatings for hard, wear resistant applications, as well as medical implants and tools. These materials have a high hardness along with wear and corrosion resistance[30-32] as well as hot corrosion resistance.[104,105] Chromium nitride is also formed in steels and provides benefits in increased hardness and toughness.[106-108]

Within the Cr-N system, there are two nitrides present: cubic CrN and hexagonal closed packed Cr_2N. Figure 2.8 shows the phase diagram of the Cr-N system with calculated isobars.[29] Cr_2N decomposes to metallic Cr and demonstrates a net loss of nitrogen content at atmospheric pressure as shown by the reaction below. However, at a pressure of 10 atm, Cr_2N can achieve a melting temperature of 1750°C. By increasing the N_2 pressure, different states of chromium nitride can be achieved.

$$2Cr_2N \rightleftharpoons 4Cr + N_{2\,(g)} \qquad \Delta G^o_{rxn} = -35.343kJ \; at \; T = 1750°C \tag{3}$$

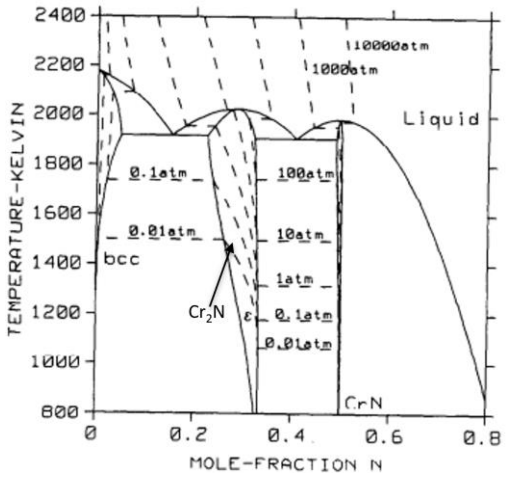

Figure 2.8: Phase diagram of the Cr-N with calculated isobars. Adapted from K. Frisk.[29]

Chromium nitride can be synthesized by multiple routes. One example is by heating Cr metal at temperatures near 1000°C in a stream of ammonia.[109] These reactions can also be completed with chromium halides or hydrides with nitrogen or ammonia.[109] A popular method for the synthesis of chromium nitrides is SHS. Cr metal powders are chosen as the starting materials, which are then pressed into pellets. The reaction is then conducted in a chamber filled with N_2 gas. The N_2 gas pressure in these reactions can vary from 0.45-4.24 MPa, as reported in the study by Yeh and Liu.[109] The increased nitrogen pressure increased the combustion temperature and the flame-front propagation velocity, enhancing the nitridation due to increased nitrogen content at the reaction front. After synthesis, billets of materials can be formed from hot pressing in a N_2 atmosphere, often at temperatures around 1300°C with pressures of 20-30 MPa.[110,111]

The melting behavior of AlON and Cr_2N have not previously been studied via aerodynamic levitation. These materials have been selected for investigation to demonstrate the benefits of hyperbaric aerodynamic levitation melting. These materials

were suitable choices for study with hyperbaric aerodynamic levitation due to AlON and Cr_2N having a dependence on high nitrogen pressure. Phase preservation and lattice parameter shifts will be investigated to determine the effect of increased nitrogen gas pressure.

PAPER

I. A HYPERBARIC AERODYNAMIC LEVITATOR FOR CONTAINERLESS MATERIALS RESEARCH

Sydney E. Boland,[1] Stephen K. Wilke,[2] Jonathan A. Scott,[1] Sarah M. Schlossberg,[2] Alex Ivaschenko,[3] Richard J.K. Weber,[2] David W. Lipke[1*]

[1)] Missouri University of Science and Technology, Department of Materials Science and Engineering, Rolla, MO, USA (*Electronic mail: lipke@mst.edu)
[2)] Materials Development, Inc., Arlington Heights, IL, USA
[3)] Encole LLC, San Jose, CA, USA

ABSTRACT

A hyperbaric aerodynamic levitator has been developed for containerless materials research at specimen temperatures exceeding 2000°C and pressures up to 10.3 MPa (1500 psi). This report describes prototype instrument design and observations of the influence of specimen size, density, pressure, and flow rate on levitation behavior. The effect of pressure on heat transfer was also assessed by studying the heating and cooling behavior of levitated Al_2O_3 liquids. A threefold increase in convective heat transfer coefficient was estimated as pressure increased to 10.3 MPa. The results demonstrate that hyperbaric aerodynamic levitation is a promising technique for containerless materials research at high gas pressures.

1. INTRODUCTION

Levitators are useful for studying solidification and vitrification phenomena of ubiquitous importance to materials that undergo solid-liquid phase transitions during their natural history or in industrial processing, and, consequently, levitators boast a strong legacy of materials discovery breakthroughs.[1-4] Researchers have used levitators to synthesize and study some of the earliest known examples of ultra-high purity semiconductors[5,6] and bulk metallic glasses.[7] Levitators have enabled advances in fundamental science by providing direct evidence of liquid-liquid phase transitions[8-11] and by elucidating high temperature structural chemistry of corrosive and hazardous materials.[12,13] Levitators serve as sample environments for synchrotron beamlines for the acquisition of atomic structure data while simultaneously probing structural chemistry via high energy x-ray scattering techniques.[3,14-20]

Levitators can attain specimen temperatures of 2000°C or greater using directed energy sources such as lasers, including continuous wave CO_2 lasers (CW CO_2), or electron beams, or via electromagnetic inductive coupling, or combinations thereof. Ambient environments in standard levitators vary from high vacuum to near-atmospheric pressures depending on the requirements of the selected heating method and instrument design limitations. As summarized in Table 1, special purpose levitators capable of hyperbaric operation (i.e., operating at greater than normal atmospheric pressure) have attained high specimen temperatures via either steady-state heating or transient dynamic pulse-heating techniques. Pulse-heating techniques can attain extreme specimen temperatures, although short (ms) heating times limit the types of measurements that can

be made. Accordingly, levitators used as sample environments for synchrotron beamlines typically employ steady-state heating techniques.

Table 1: Overview of hyperbaric levitators used for containerless materials research.

Principle of Levitation	**Heating Source**	**Max. Specimen Temperature [°C]**	**Max. Operating Pressure [MPa]**	**Reference**
Acoustic	Laser (CW CO_2)	1300	0.9	[21]
Acoustic	Jacketed chamber	180	20	[22]
Acoustic	Laser (pulsed CO_2)	5000	30	[23,24]
Aerodynamic	Laser (CW CO_2)	2200	10.3	This work
Hybrid Aerodynamic Electrostatic	Laser (CW CO_2)	2000	1	[25,26]
Buoyant	Radiant heater (HIP)	1800	200	[27]
Electrostatic	Laser (CW CO_2)	2700	0.3	[28]
Electromagnetic	Induction	1600	10	[29]
Electromagnetic	Induction	1900	5	[30]

Containerless experimentation at high gas pressures confers two primary benefits. First, pressurized systems are known to suppress volatilization. For example, when limited by mass transport through an external boundary layer, evaporation rates are proportional to $1/\sqrt{P}$ up to a critical pressure on the order of 1-100 MPa.[31,32] With reduced volatile losses, specimen composition can be better preserved. Specimens may also be observed for longer durations, enabling measurements of properties and/or structural chemistry of highly volatile materials. Second, reactive gas pressures possess

increased chemical potentials $\Delta\mu_i = RT \ln f_i/f_i^\circ$ where i is a reactive species (e.g., oxygen or nitrogen) whose magnitude may attain ca. 100 kJ/mol at elevated temperatures. This increase in chemical potential can dramatically affect phase equilibria, a fact that has been exploited to synthesize new compounds using elevated pressure crystal growth, surface heating and/or melting.[33-43]

This work describes the design and performance characteristics of a prototype hyperbaric aerodynamic levitator for containerless materials research. The levitation behaviors of two series of spherical specimens of varying size and density were studied as functions of pressure and flow rate. Additionally, the effect of pressure on heat transfer was assessed by comparing the heating and cooling behaviors of levitated liquid Al_2O_3 at pressures up to 10.3 MPa.

2. INSTRUMENT DESCRIPTION

The hyperbaric aerodynamic levitator shown in Figure 1 comprises four major components: a pressure vessel; a diamond window for CO_2 laser admittance; a converging-diverging conical nozzle; and pressurized fluid handling systems. System components and controls were carefully engineered for safe operation. The pressure vessel (Encole LLC, San Jose, CA, USA) consists of a monolithic CNC machined billet of 7075-T6 aluminum featuring a vertical through-bore, multiple ports, and internal water-cooling passages. Finite element simulations were conducted to design the pressure vessel for a maximum internal pressure of 17.2 MPa (2500 psi) with a safety factor of four. A pressure-relief valve and burst disc were installed on the outlet and inlet sides of

the pressure vessel, respectively. As an additional engineering control, operators were in a separate room from the hyperbaric levitator. The electronic backpressure regulator and mass flow controllers were operated via computer interface with remote displays.

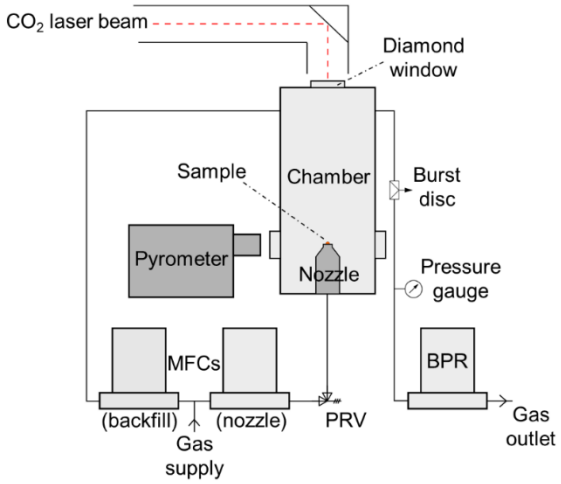

Figure 1: Schematic of prototype hyperbaric aerodynamic levitator integrated with a CO_2 laser. Abbreviations: mass flow controllers (MFCs), back pressure regulator (BPR), pressure relief valve (PRV).

The converging-diverging levitation nozzle features conical semi-angles of 30°-60° intersecting at a cylindrical orifice whose diameter may vary from 0.5-2 mm.[20] The nozzle was vertically installed and sealed onto the pressure vessel with an SAE thread identical to that used for the sight glasses. The shallow conical nozzle design allowed for about half of the levitated specimen volume to be visible above the top of the nozzle as viewed from the horizontal sight glasses. During levitation experiments, the specimen was remotely viewed via camera (acA150-uc, Basler) equipped with 1.0X f/6-f/25 telecentric lens (Edmund Optics, Inc.) using a white LED backlight. The optical configuration provided a spatial resolution of 4.8 µm x 4.8 µm per pixel and videos were

recorded with a frame rate of 150 fps. Levitation stability as indicated by the vertical displacement of the top of the sphere was measured using motion tracking software (ProAnalyst, Xcitex Inc.).

A pair of mass flow controllers (SLA5850 Series, Brooks Instrument) independently provided pressurized fluid to the levitation nozzle (maximum volumetric flow rate Q = 5.0 SLM) and as a purge flow across the diamond window to abate deposit formation (max. Q = 0.5 SLM). Pressure within the chamber was controlled using an electronic backpressure regulator (SLA5820 Series, Brooks Instrument) located downstream of the pressure vessel outlet. During a typical levitation experiment, the purge flow was maintained at a constant 0.5 SLM until the system attained the ambient pressure setpoint. Flow through the conical nozzle was then increased until maximum flow rate was attained or instabilities in specimen position presenting as lateral movement were observed. Subsequently, levitation height was recorded at different flow rates stepping down in increments of 0.1 SLM until the sphere no longer displayed stable levitation. In this investigation, two series of levitation experiments were conducted: aluminum spheres of varying diameter (2.529, 3.048, 3.575, or 3.979 mm) and 3 mm diameter spheres made from materials of varying density (aluminum – 2.71 g/cm^3, alumina (Al_2O_3) – 3.95 g/cm^3, yttria-stabilized zirconia (YSZ) – 6.00 g/cm^3, or type 302 stainless steel (SS302) – 7.93 g/cm^3).

A custom sight glass featuring a 1.3 mm thick x 10 mm clear aperture diamond window (Element Six Technologies, Santa Clara, CA, USA) encased in a SAE-12 fitting made from 17-4PH steel (Encole, LLC). All sight glass housings featured SAE threads coated with WS_2 in accordance with AMS2530 to prevent galling during frequent

disassembly. The diamond window provides excellent transmission for the 10.6 μm wavelength CW CO_2 laser (400 W Synrad Firestar i401, Novanta Photonics) used as heating source in these studies. Diamond is an ideal material for this purpose given its excellent thermal conductivity and high strength as compared to traditional CO_2 laser window materials such as ZnSe. In this work the diamond window was uncoated; consequently, approximately one-third of incident laser energy was lost due to Fresnel reflections (i.e., diamond has an index of refraction of 2.376 at 10.6 μm).

3. HYPERBARIC AERODYNAMIC LEVITATION

Figure 2 shows the effect of volumetric flow rate Q on stable levitation height of the specimen Z normalized to its diameter d at selected pressures of 3.45 MPa (corresponding to a nitrogen density of 55.5 kg/m^3) and 10.3 MPa (corresponding to a nitrogen density of 166.6 kg/m^3). From available data it is recognized that Z/d increases with Q (at a fixed pressure and specimen density) and decreases with specimen density (at a fixed pressure and flow rate). Deviations from these trends are discernable. For example, an increase in Z/d when Q approaches 3.0 SLM at 10.3 MPa is observed for the 2.529 mm, 3.048 mm, and 3.575 mm diameter aluminum spheres that is not seen for larger diameter aluminum spheres. Similarly, an increase in Z/d when Q approaches 3.0 SLM at 10.3 MPa is observed for the 3.000 mm diameter aluminum sphere, but not for this same sphere at 3.45 MPa and not for 3.000 mm diameter spheres made from denser materials at either pressure. These results suggest that a change in drag force occurs

across this flow rate regime whose magnitude is sufficient to displace the stable levitation position of relatively lightweight specimens.

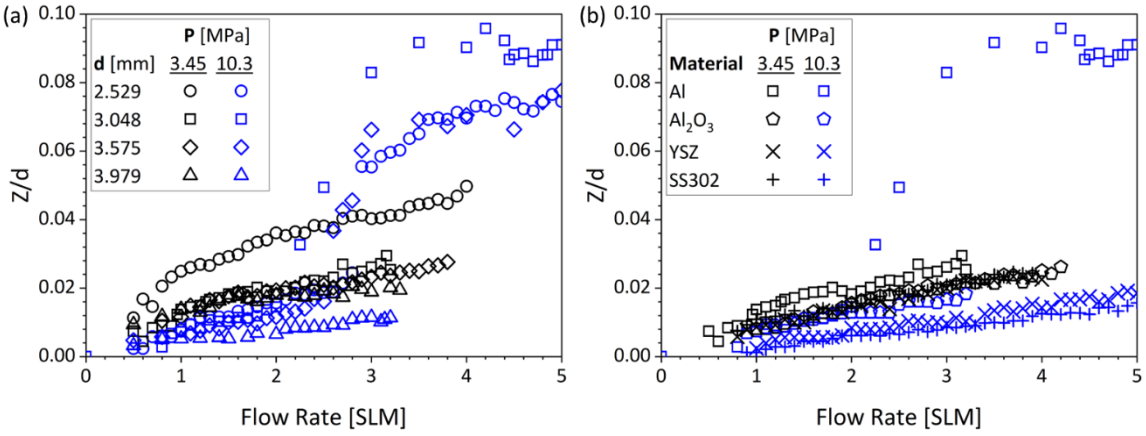

Figure 2: Relative stable levitation position (Z/d) vs. volumetric flow rate (SLM) for experimental series varying (a) diameter for Al specimens and (b) material (aluminum – 2.71 g/cm^3, alumina (Al_2O_3) – 3.95 g/cm^3, yttria-stabilized zirconia (YSZ) – 6.00 g/cm^3, or type 302 stainless steel (SS302) – 7.93 g/cm^3) for 3.000 mm diameter spheres.

To better understand observed trends, fluid mechanics relations were used to calculate drag force for varying experimental conditions. A necessary condition for aerodynamic levitation is given by the force balance:

$$\sum F_z = 0 = F_d + F_{\nabla P} + F_b - F_g \cong F_d - F_w \quad (1)$$

where F_d is drag force, $F_{\nabla P}$ is pressure gradient force, F_b is buoyant force, F_g is the force of gravity, and $F_w = F_g - F_b$ is the buoyant weight of the sphere. The buoyant weight must therefore be offset by the sum of the drag force and pressure gradient force. For clarity, herein we neglect the pressure gradient force, as it is assumed the full pressure drop of the fluid jet occurs within the nozzle orifice (a detailed simulation would be needed to confirm this assumption).

The buoyant weight of a spherical specimen can be expressed in terms of specimen size (d), specimen density (ρ_s), fluid density (ρ), and acceleration due to gravity (g) as:

$$F_w = \frac{1}{6}\pi d^3(\rho_s - \rho)g \tag{2}$$

The drag force can be expressed as the product of the drag coefficient C_d, specimen area, and dynamic pressure:

$$F_d = C_d \cdot \frac{1}{2}\rho\left(\frac{\pi d^2}{4}\right)\mathrm{v}^2 \tag{3}$$

In equation (3), velocity v is not singular valued but rather varies with axial position as the flow diverges from the conical nozzle exit. The axial flow velocity can be taken to be inversely proportional to the vertical distance from the jet source[44], or:

$$\mathrm{v}^2 = \left(\frac{A}{Z}\right)^2 \tag{4}$$

where A is a constant of dimensions length × velocity. Substitution of (4) into (3) yields:

$$F_d = C_d \cdot \frac{1}{8}\pi\rho\frac{A^2}{\left(\frac{Z}{d}\right)^2} \tag{5}$$

The constant A can be determined by conservation of momentum flux by assuming the jet momentum J crossing any longitudinal surface located at distance Z away from the jet source is constant. The jet momentum at the nozzle exit J_{nozzle} is therefore related to the constant A by the expression:[44]

$$J_{nozzle} = \frac{1}{2}\rho\left(\frac{\pi D^2}{4}\right)\mathrm{v}_{nozzle}^2 = \pi\rho A^2\beta^2 \tag{6}$$

where β is the cone angle of the jet, here assumed to be the same as the nozzle, and D is the diameter of the nozzle orifice. Re-arranging, the constant A is given by:

$$A^2 = \frac{\mathrm{v}_{nozzle}^2 D^2}{8\beta^2} \tag{7}$$

The nozzle velocity can be expressed in terms of the experimental parameters volumetric flow rate (Q), fluid density, and nozzle cross-sectional area:

$$\mathrm{v}_{nozzle} = \frac{Q}{\rho(\frac{\pi D^2}{4})} \tag{8}$$

Substitution of (8) into (7) yields:

$$A^2 = \frac{2Q^2}{\pi^2 \rho^2 D^2 \beta^2} \tag{9}$$

Finally, substitution of (9) into (5) and equating to (2) yields the following expression for drag coefficient upon simplification and re-arrangement:

$$C_d = \frac{2\pi^2 \left(\frac{Z}{d}\right)^2 d^3(\rho_s - \rho) g \rho D^2 \beta^2}{3Q^2} \tag{10}$$

Evaluating expression (10) using observed relative levitation heights as functions of flow rate and fluid density (i.e., pressure) yields computed drag coefficient values as shown in Figures 3 for specimens of changing size and as shown in Figure 4 for specimens of varying density. Specific fluid densities of interest are highlighted in color and act as representative trends, while all other conditions are shown in gray. Atmospheric pressure, 3.45 MPa, and 10.3 MPa are highlighted for all samples of varying size and density, while the transitions between trends is also highlighted when applicable.

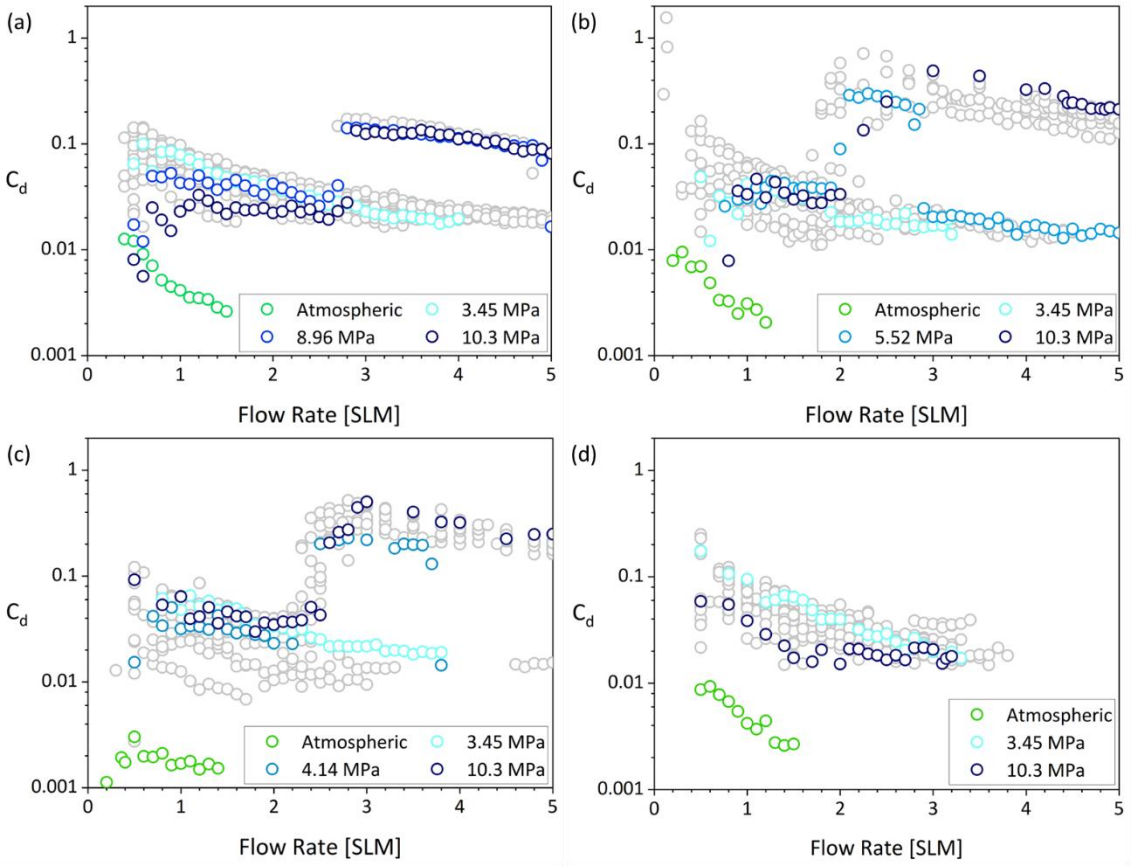

Figure 3: Computed drag coefficients for Al specimens with diameters of (a) 2.529 mm, (b) 3.048 mm, (c) 3.575 mm, (d) 3.979 mm as a function of volumetric flow rate. Highlighted pressure series correspond to minimum and maximum pressures employed in this work, a selected common trend for comparison, and, where applicable, the pressure at which deviation in the trends first appears.

Figures 3 and 4 illustrate the occurrence of two drag coefficient regimes: a primary trendline onto which most observations fall and a secondary trendline that reflects the change in relative levitation height for lightweight samples (i.e., small size and/or low density) at moderate flow rates and high pressures. For example, Figure 3a shows a jump in computed C_d values near 3.0 SLM for pressures exceeding 8.96 MPa. Observations fall on secondary trendlines for similar flow rates starting at pressures of 5.52 MPa and 4.14 MPa, as shown respectively in Figures 3b and 3c, with increasing

specimen diameter. The transitional nature of these drag coefficient regimes are captured in the highlighted pressure series at 5.52 MPa in Figures 3b and 3c, where the calculated C_d deviates from the primary trendline up to the secondary trendline before returning to the primary trendline at higher flow rates.

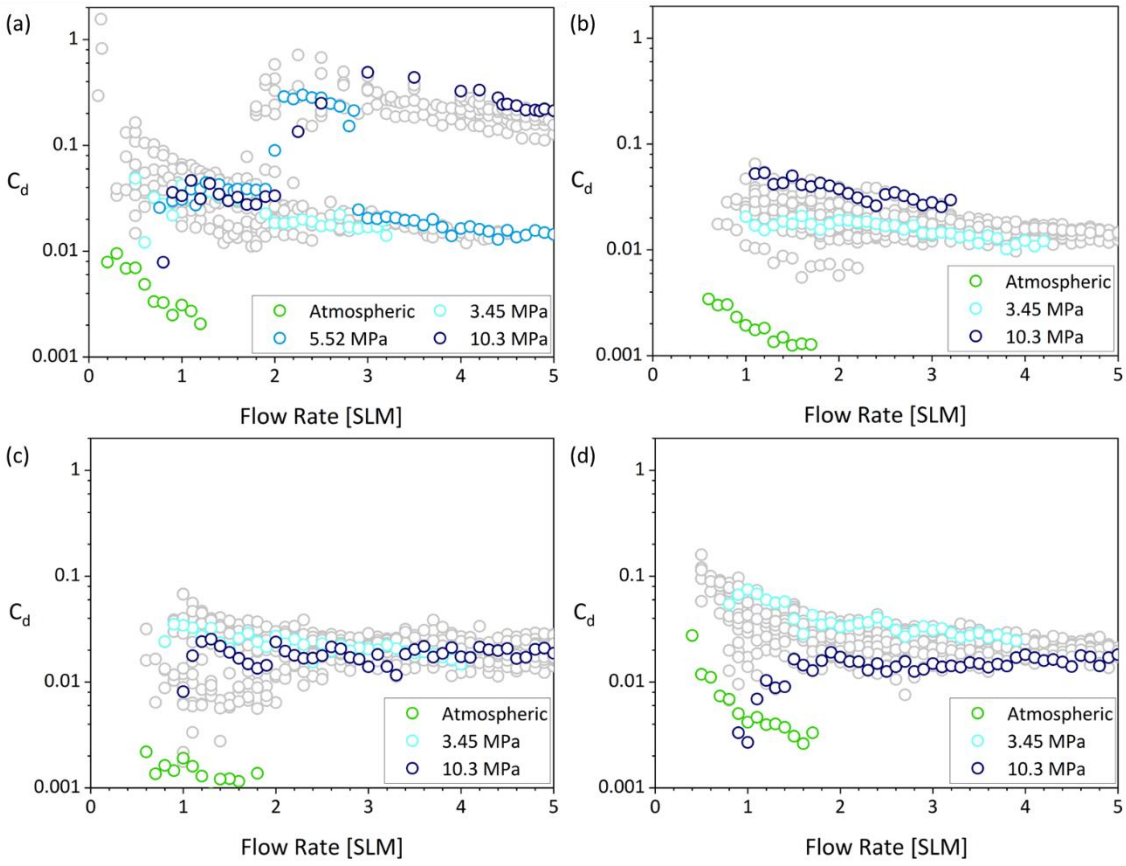

Figure 4: Computed drag coefficients for 3.000 mm diameter specimens Al specimens made from (a) Al, (b) Al_2O_3, (c) YSZ, (d) SS302 as a function of volumetric flow rate. Highlighted pressure series correspond to minimum and maximum pressures employed in this work, a selected common trend for comparison, and, where applicable, the pressure at which deviation in the trends first appears.

An alternative means to identify the onset of the secondary trendline employs a semi-empirical dimensionless scaling relation to describe the suspension of spheres in turbulent jets:

$$\left(\frac{C_d}{3}\right)^{1/2} Fr \left(\frac{\rho_s}{\rho}\right)^{-1/2} \left(\frac{d}{D}\right)^{-3/2} = \left(\frac{Z}{D}\right)^{1/\alpha} \tag{11}$$

where Fr is Froude number ($Fr = \mathrm{v}/\sqrt{Dg}$).[45,46] This expression was used to numerically fit the free parameter α using the data from Figures 3 and 4 as summarized in Figure 5:

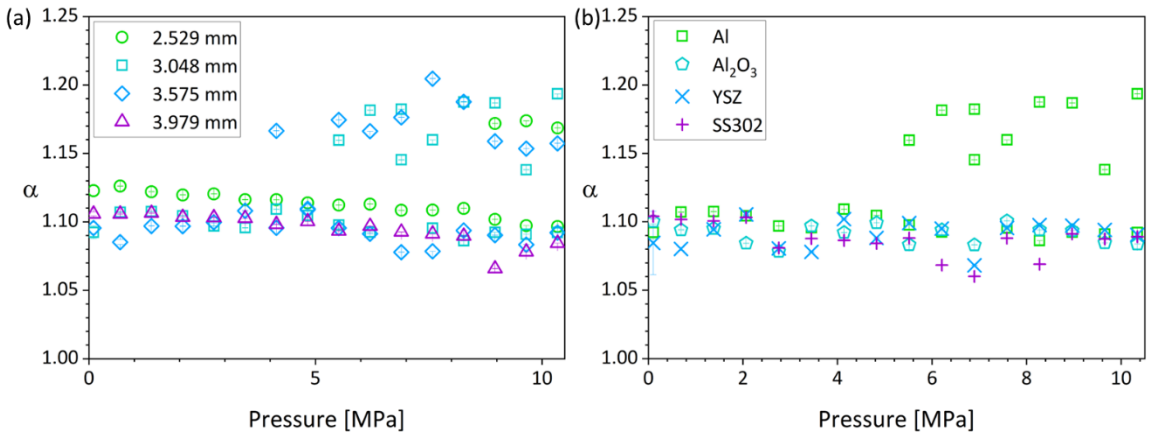

Figure 5: Best fit α values with error bars for trends illustrated in Figures 3 and 4 for varying specimen (a) size and (b) material at pressures ranging from atmospheric to 10.3 MPa.

As shown in Figure 5, the secondary trendline for lightweight specimens features a statistically different exponential dependence on experimental parameters as compared to the primary trendline. The origin of this difference is not well understood but is speculated to relate to wake turbulence transitions like those reported for spheres in comparable Reynolds and Froude number regimes.[4]

The effect of fluid density was also evaluated by comparing hyperbaric aerodynamic levitation behavior in nitrogen versus argon as a function of pressure. Figure 6 illustrates levitation of 3.000 mm Al_2O_3 spheres at 3.45 MPa (Ar – 55.5 kg/m^3, N_2 – 39.8 kg/m^3) and 10.3 MPa (Ar – 166.6 kg/m^3, N_2 – 118.7 kg/m^3). At each pressure, the heavier fluid imparts more momentum to the sphere, resulting in a higher relative levitation height. As pressure increases – and, consequently, flow velocity decreases at any given flow rate – relative levitation heights decrease for both fluids.

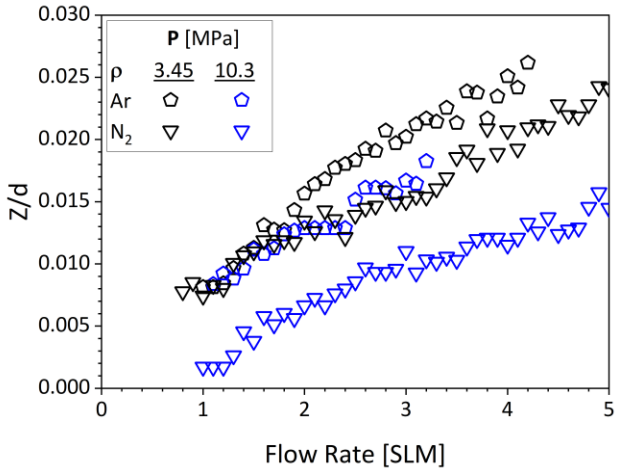

Figure 6: Relative stable levitation height vs. volumetric flow rate for a 3.000 mm Al_2O_3 sphere using argon or nitrogen as levitation fluid at selected pressures of 3.45 MPa and 10.3 MPa.

4. HEAT TRANSFER IN A DENSE FLUIDIZING MEDIA

A levitated 3.000 mm Al_2O_3 sphere was melted with a 400 W CO_2 laser at atmospheric pressure, 2.07 MPa, 4.14 MPa, 6.21 MPa, 8.27 MPa, and 10.3 MPa nitrogen to assess the effect of pressure on heat transfer characteristics. Levitation trials were

conducted with a constant volumetric flow rate of 1.5 SLM at ambient pressures up to 4.14 MPa and at a constant volumetric flow rate of 3.5 SLM for ambient pressures from 6.21 MPa to 10.3 MPa, with flow rates selected to maximize specimen stability during heating.

Figure 7 shows the molten Al_2O_3 sphere levitated at atmospheric pressure and at 10.3 MPa. At elevated pressures the increased fluid density apparently leads to concomitant change in fluid refractive index, thereby allowing for the turbulent flow structure to be visualized. Figure 8 shows cooling curves for the 3.000 mm Al_2O_3 sphere as measured by optical pyrometry (IR-CAS, Chino Corp.). Reported apparent temperatures are uncorrected for effects of view factor, specimen emissivity, or window absorption.

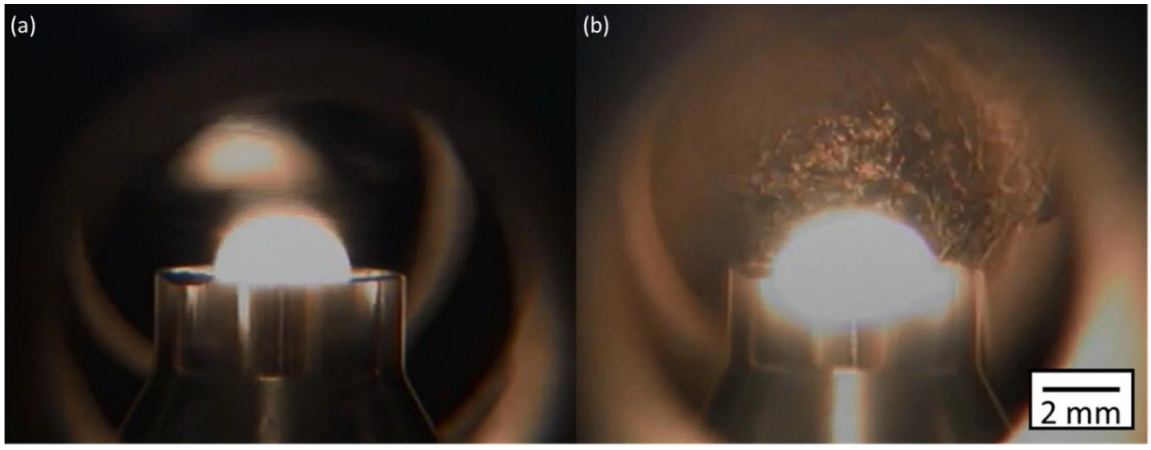

Figure 7: Aerodynamically levitated molten Al_2O_3 droplet (initially 3.000 mm diameter sphere) at (a) atmospheric pressure and (b) at 10.3 MPa. At atmospheric pressure a reflection of the sample by a window surface is clearly visible. At high pressure, strong convection results in a turbulent wake pattern in the fluid above the hot sample as well as blurring of the image. (Multimedia view).

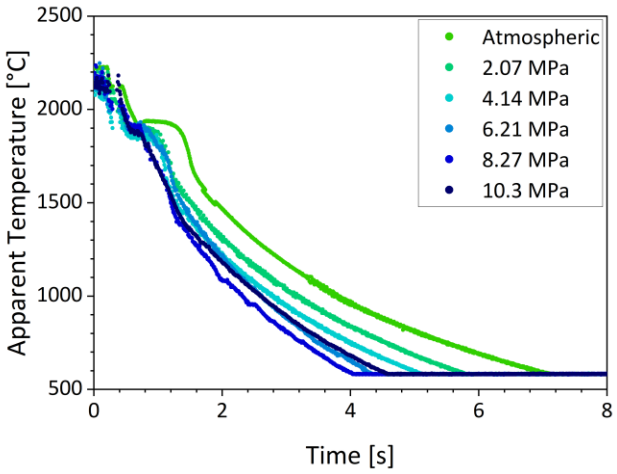

Figure 8: Cooling curves of levitated Al_2O_3 liquids as recorded by optical pyrometry as a function of nitrogen pressure.

Convective heat transfer coefficients h were calculated from cooling curve data by fitting the following convection-radiation heat equation:

$$\rho_s c_p \left(\frac{\pi d^3}{6}\right)\frac{dT}{dt} + \pi d^2[h(T - T_\infty) + \varepsilon\sigma(T^4 - T_\infty^4)] = 0 \qquad (12)$$

Calculations assumed specimen emissivity of ε = 0.9, constant sample density, and utilized reported literature values for temperature-dependent heat capacity. Resulting values are summarized in Table 2 where convective heat transfer coefficient is shown to increase threefold as pressure increased from atmospheric pressure to 10.3 MPa.

The convective-radiative heat balance can be used to estimate maximum attainable specimen temperatures as a function of absorbed laser energy and specimen surface area. Figure 9 shows calculated equilibrium temperatures using estimated heat transfer coefficients for atmospheric pressure aerodynamic levitation (dashed) and hyperbaric aerodynamic levitation (solid). Assuming a constant 150 W output laser power and total hemispherical emissivity of 0.9, specimen temperatures above 2100°C

should be attainable for 3.0 mm specimens with absorptivity values greater than 0.6 at 10.6 μm. To attain higher specimen temperatures, additional laser energy must be delivered to the sample, which can likely be achieved via combination of optimization of beam delivery optics, the use anti-reflective coatings on the diamond window used for laser admittance, or increasing output laser power.

Table 2: Convective heat transfer coefficient calculated from cooling curve data for a 3.000 mm Al_2O_3 sphere at varying MPa pressures.

Pressure (MPa)	**h (W/m^2K)**
Atmospheric	300 ± 200
2.07	500 ± 300
4.14	500 ± 200
6.21	700 ± 200
8.27	700 ± 200
10.3	900 ± 200

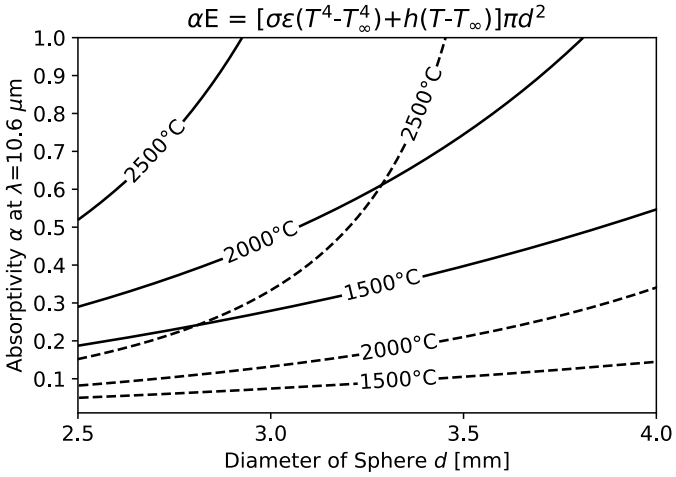

Figure 9: Calculated equilibrium temperature versus specimen size using heat balance equation shown. *E* is output laser power (150 W), *h* is convective heat transfer coefficient (solid lines: 900 W/m^2K, dashed lines: 300 W/m^2K).

Concordant with increased convective heat losses, additional laser power was required to melt the specimen. Figure 10 compares the laser power necessary to overcome convective heat losses for atmospheric pressure aerodynamic levitation versus hyperbaric aerodynamic levitation at 10.3 MPa. An increase of approximately 15% of the maximum laser power corresponding to an additional 60 W was required to attain molten Al_2O_3 at 10.3 MPa. This represents a modest increase relative to the total laser power available (400 W maximum), indicating that materials with even greater melting points than Al_2O_3 can be levitation melted in hyperbaric conditions, demonstrating the feasibility of melting a wide range of specimens at hyperbaric conditions (note: as temperatures increase further above 2000°C, radiative heat losses are expected to dominate over convective heat losses such that increased convective heat losses at elevated pressures may become negligible).

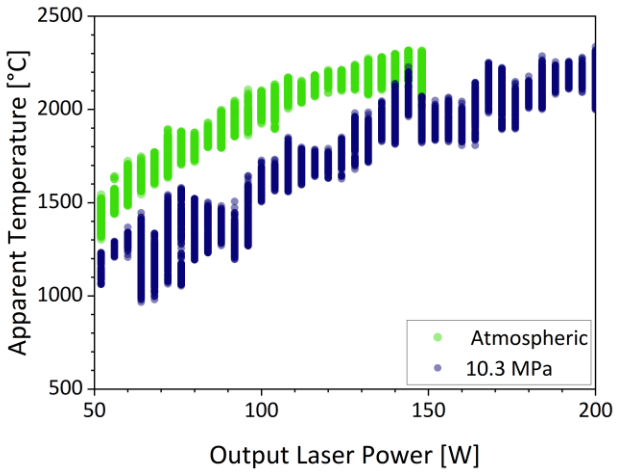

Figure 10: Apparent temperature vs. output laser power necessary to attain melting of a 3.000 mm Al_2O_3 sphere in nitrogen at atmospheric pressure and at 10.3 MPa.

5. CONCLUSION

A hyperbaric aerodynamic levitator for containerless materials research has been designed and tested. The instrument operates at ambient pressures up to 10.3 MPa and can attain specimen temperatures greater than 2100°C depending on material characteristics. Preliminary evaluations of hyperbaric aerodynamic levitation phenomena indicate stable levitation can be attained across a wide range of flow rates and pressures. For the nozzle configuration tested, two stable levitation regimes were observed for lightweight specimens that are speculated to be associated with a change in turbulent wake structure. Additional simulation and experimentation are recommended to better understand the effects of flow turbulence on levitation stability.

Output laser power necessary to melt specimens at elevated pressures increased due to enhanced convective heat transfer with increasing fluid density; however, the magnitude was modest – approximately 60 W additional output laser power in going from atmospheric pressure to 10.3 MPa flowing nitrogen necessary to melt a 3.000 mm Al_2O_3 sphere. The results demonstrate that hyperbaric aerodynamic levitation is a promising technique for containerless materials research at high gas pressures. The extended instrument operating conditions in temperature-fugacity space are expected to confer two primary benefits for future experimentation: suppressing volatile losses and accessing new chemical stability regions especially for oxide and/or nitride compositions via use of high reactive gas pressures.

6. AUTHOR CONTRIBUTIONS

Sydney E. Boland: Methodology, validation, formal analysis, investigation, writing – original draft, writing – review & editing, visualization. Stephen K. Wilke: Methodology, investigation, visualization, writing – review & editing. Jonathan A. Scott: Methodology. Sarah M. Schlossberg: Investigation, visualization. Alex Ivaschenko: Resources, writing – review & editing. Richard J.K. Weber: Methodology, investigation, resources, writing – review & editing, supervision, funding acquisition. David W. Lipke: Conceptualization, methodology, writing – review & editing, supervision, project administration, funding acquisition.

7. ACKNOWLEDGMENTS

The authors gratefully acknowledge partial financial support for author Sydney E. Boland from the Office of Naval Research (ONR) Naval Engineering Education Consortium (NEEC) Grant No. N00174-21-1-0008. Funding assistance from the College of Engineering and Computing and the Materials Research Center at Missouri University of Science and Technology is gratefully acknowledged. The authors are thankful for contributions from undergraduate students Brennan Long (Missouri S&T) and Gerald Amory (Morgan State University) for their assistance in early instrument development. We also extend sincere thanks to Professor Mario Affatigato (Coe College) for assistance with prototype testing and stimulating discussions.

8. DATA AVAILABILITY STATEMENT

The data that support the findings of this study are available from the corresponding author upon reasonable request.

APPENDIX

Table A.1: List of Abbreviations.

Abbreviation	Term
d	diameter of sphere
D	diameter of nozzle
ρ_s	density of sphere
ρ	density of fluid
Z/d	relative levitation height
g	standard acceleration due to gravity
v	Velocity
Q	volumetric flow rate
C_d	drag coefficient
A	momentum flux constant
β	cone angle of the nozzle
Fr	Froude number
h	convective heat transfer coefficient
c_p	heat capacity
ε	Emissivity
σ	Stefan-Boltzmann constant

REFERENCES

1. E.H. Brandt. Science 243, 349 (1989).

2. M. Barmatz. MRS Proc. 9, 25 (1981).

3. D.M. Herlach, R.F. Cochrane, I. Egry, H.J. Fecht, A.L. Greer. Int. Mater. Rev. 38, 273 (1993).

4. R. Weber, S.K. Wilke, C.J. Benmore. J. Phys. Soc. Jpn. 91, 091008 (2022).

5. E.C. Okress, D.M. Wroughton, G. Comenetz, P.H. Brace, J.C.R. Kelly. J. Appl. Phys. 23, 545 (1952).

6. G.R. Davies. Metall. Rev. 10, 173 (1965).

7. W.K. Rhim, S.K. Chung, D. Barber, K.F. Man, G. Gutt, A. Rulison, R.E. Spjut. Rev. Sci. Instrum. 64, 2961 (1993).

8. P.F. McMillan, M. Wilson, M.C. Wilding, D. Daisenberger, M. Mezouar, G.N. Greaves. J. Phys. Cond. Matter 19, 415101 (2007).

9. G.N. Greaves, M.C. Wilding, S. Fearn, D. Langstaff, F. Kargl, S. Cox, Q. Vu Van, O. Majérus, C.J. Benmore, R. Weber, C.M. Martin, L. Hennet. Science 322, 566 (2008).

10. J.J.Z. Li, W.K. Rhim, C.P. Kim, K. Samwer, W.L. Johnson. Acta Mater. 59, 2166 (2011).

11. S. Wei, F. Yang, J. Bednarcik, I. Kaban, O. Shuleshova, A. Meyer, R. Busch. Nat. Comm. 4, 2083 (2013).

12. S. Krishnan, S. Ansell, J.J. Felten, K.J. Volin, D.L. Price. Phys. Rev. Lett. 81, 586 (1998).

13. L.B. Skinner, C.J. Benmore, J.K.R. Weber, M.A. Williamson, A. Tamalonis, A. Hebden, T. Wiencek, O.L.G. Alderman, M. Guthrie, L. Leibowitz, J.B. Parise. Science 346, 984 (2014).

14. G. Jacobs, I. Egry, K. Maier, D. Platzek, J. Reske, R. Frahm. Rev. Sci. Instrum. 67, 3683 (1996).

15. C. Landron, X. Launay, J.C. Rifflet, P. Echegut, Y. Auger, D. Riffier, J.P. Coutures, M. Lemonier, M. Gailhanou, M. Bessiere, D. Bazin, H. Dexpert. Nucl. Instrum. and Methods in Phys. Res. B124, 627 (1997).

16. S. Krishnan, J.J. Felten, J.E. Rix, J.K.R. Weber, P.C. Nordine, M.A. Beno, S. Ansell, D.L. Price. Rev. Sci. Instrum. 68, 3512 (1997).

17. P.F. Paradis, T. Ishikawa, J. Yu, S. Yoda. Rev. Sci. Instrum. 72, 2811 (2001).

18. L. Hennet, D. Thiaudière, M. Gailhanou, C. Landron, J.P. Coutures, D.L. Price. Rev. Sci. Instrum. 73, 124 (2002).

19. L. Hennet, I. Pozdnyakova, A. Bytchkov, V. Cristiglio, P. Palleau, H.E. Fischer, G.J. Cuelle, M. Johnson, P. Melin, D. Zanghi, S. Brassamin, J.F. Brun, D.L. Price. Rev. Sci. Instrum. 77, 053903 (2006).

20. J.K.R. Weber, A. Tamalonis, C.J. Benmore, O.L.G. Alderman, S. Sendelbach, A. Hebden, M.A. Williamson. Rev. Sci. Instrum. 87, 073902 (2016).

21. C.A. Rey, R. Sisler, D.R. Merkley, T.J. Danley. Prog. Astronaut. Aeronaut. 127, 270 (1990).

22. D. Borosa, S. Kareth, M. Petermann. Chem. Ing. Tech. 84, 145 (2012).

23. J. Magill, F. Capone, R. Beukers, P. Werner, R.W. Ohse. High Temp.-High Pressures 19, 461 (1987).

24. R.W. Ohse. Int. J. Thermophys. 11, 753 (1990).

25. M.V. Kumar, J.T. Okada, T. Ishikawa, P.F. Paradis, Y. Watanabe. Meas. Sci. Technol. 25, 085301 (2014).

26. P.F. Paradis, T. Ishikawa, J. Yu, S. Yoda. Rev. Sci. Instrum. 72, 2811 (2001).

27. M. Nakoto, K. Ishizaki. Proc. MRS Symp. 251, 47 (1991).

28. J.R. Rogers, R.W. Hyers, T. Rathz, L. Savage, M.B. Robinson. AIP Conf. Proc. 552, 332 (2001).

29. N.H. El-Kaddah, D.G.C. Robertson. Metall. Trans. B, 9B, 191 (1978).

30. Ts.V. Rashev, R.I. Ivanov, L. Saraiyanov. Zavod. Lab., 44, 550 (1978).

31. M. Chesswas, B. Cockayne, D.T.J. Hurle, E. Jakeman, J.B. Mullin. J. Crystal Growth 11, 225 (1971).

32. J.S. Haggerty, J.L. O'Brien, J.F. Wenckus. J. Crystal Growth 3/4, 291 (1968).

33. L.C.F. Blackman, P.H. Dundas, A.W. Moore, A.R. Ubbelohde. Brit. J. Appl. Phys. 12, 377 (1961).

34. H. Van Hook, Rev. Sci. Instrum. 36, 1119 (1965).

35. A.R. Bradshaw, D. Fort. Rev. Sci. Instrum. 63, 5459 (1992).

36. C. Ronchi, J.P. Hiernaut, R. Selfslag, G.J. Hyland. Nucl. Sci. Eng. 113, 1 (1993).

37. S. Möhr, H. Müller-Buschbaum. Angew. Chem. Int. Ed. Engl. 34, 634 (1995).

38. S. Hosokawa, W.C. Pilgrim. Rev. Sci. Instrum. 72, 1721 (2001).

39. D. Manara, C. Ronchi, M. Sheindlin. Int. J. Thermophys. 23, 1147 (2002).

40. D. Manara, M. Sheindlin, W. Heinz, C. Ronchi. Rev. Sci. Instrum. 79, 113901 (2008).

41. F. De Bruycker, K. Boboridis, R.J.M. Konings, M. Rini, R. Eloirdi, C. Guéneau, N. Dupin, D. Manara. J. Nucl. Mater. 419, 186 (2011).

42. J.L. Schmehr, M. Aling, E. Zoghlin, S.D. Wilson. Rev. Sci. Instrum. 90, 043906 (2019).

43. W.A. Phelan, J. Zahn, Z. Kennedy, T.M. McQueen, J. Solid State Chem. 270, 705 (2019).

44. K.T. McDonald. Am. J. Phys. 68, 388 (2000).

45. T. Barois, G. Ricard, V. Champain, L. Gey, H. Kellay. Phys. Fluids 32, 045111 (2020).

46. S. Davoust, L. Jacquin. Sixth Int. Symp. Turbulence and Shear Flow Phenomena, 1237 (2009).

47. Q. Lin, W.R. Lindberg, D.L. Boyer, H.J.S. Fernando. J. Fluid Mech. 240, 315 (1992).

II. THE MELTING OF ALUMINUM OXYNITRIDE IN A HYPERBARIC AERODYNAMIC LEVITATOR

1. INTRODUCTION

Aluminum oxynitride (AlON – $Al_{23}O_{27}N_5$) is a solid solution from the Al_2O_3-AlN system with a cubic spinel crystal structure as shown in Figure 1.[1] The γ-AlON phase, according to the phase diagram of the Al_2O_3-AlN system from McCauley and Corbin,[2] is centered on 35.7 mol% AlN and will congruently melt at 2165°C at 0.1 MPa. AlON applications include transparent armors, missile domes, and lenses due its optical transparency in the ultraviolet to infrared range.[3] AlON has a > 80% transmittance in the wavelength range from ultraviolet to mid-infrared light, as well as excellent mechanical properties.[3] Commercially produced AlON is reported to have grain sizes on the order of 150-200 μm and relative densities greater than 95%.[4]

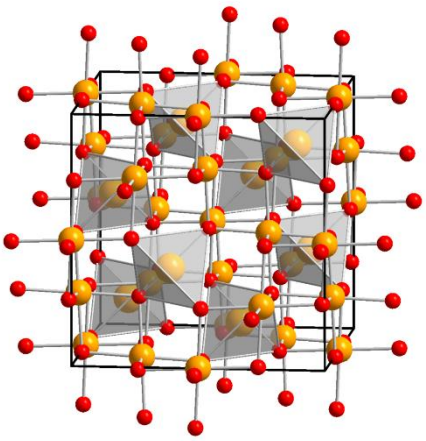

Figure 1: AlON cubic spinel crystal structure. Adapted from S.A.T Redfern et al.[1]

AlON is often referred to as nitrogen stabilized cubic aluminum oxide with 8 Al cations in tetrahedral sites and 15 Al cations and one vacancy in the octahedral sites.[5] The model shown is a unit cell with 32 anions total. This accounts for the AlON (x=5) phase and is as follows: $Al_{(64+x)/3}\,\square_{(8-x)/3}\,O_{(32-x)}\,N_x$.[5] This model shows that as N substitutions increase, the vacancy content decreases which affects the lattice stability and the lattice parameter.

There is also a dependence on the lattice parameter with N_2 pressure at temperatures greater than 2000°C.[5] A decrease in the nitrogen content or a shift in composition towards the Al_2O_3 side of the pseudo-binary phase diagram is signified by a reduced lattice parameter.[5] An increase in the nitrogen content corresponds with a decrease in the oxygen content, and this change in the ratio can be reflected in the lattice parameter. A decrease in the nitrogen content has been observed with an increase in the N_2 pressure, possibly attributed to the suppression of the oxygen rich vapor phase, Al_2O, with increased pressure.[6]

AlON was chosen to be studied as it is one of the most stable oxynitrides due to the material not fully decomposing at atmospheric pressure. By changing the N_2 gas pressure, it is expected that there will be a shift in the lattice parameter and potentially a different phase composition depending on the gaseous environment. The goal of this study was to utilize a hyperbaric aerodynamic levitator to examine the effect of N_2 pressure on phase formation and lattice parameters. AlON specimens were melted at atmospheric pressure and 10.3 MPa in N_2, as well as at atmospheric pressure in air.

2. MATERIALS PREPARATION

To produce phase pure AlON samples, there are multiple processing routes; however, the reaction sintering of Al_2O_3 and AlN was chosen for this study. The raw materials used for the synthesis of AlON were 64.3 mol% Al_2O_3 (BeanTown Chemical 99.95 wt.%, alpha phase) and 35.7 mol% AlN (BeanTown Chemical). Powders were ball milled for 24 hours with 3 mm alumina media in an ethanol medium. Once dried, the powders were compacted and pressed into 13 mm diameter pellets with a pressure of 280 MPa. Pellets were sintered in a graphite furnace with a heating rate of 10°C/min at 1950°C for 4 hours with a cooling rate of 10°C/min. Pellets were placed in a graphite crucible lined with boron nitride sprayed GraFoil (NeoGraf) to reduce contact with graphite and possible carbon contamination. Furthermore, the pellets were immersed in a powder bed of Al_2O_3 and AlN powder. Figure 2 shows the resulting pellets were phase pure AlON.

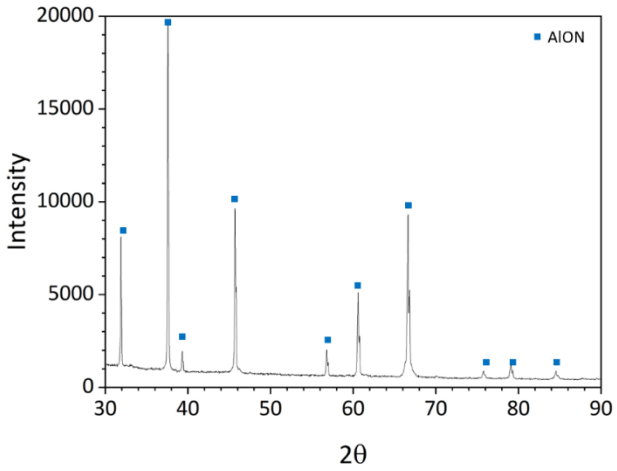

Figure 2: XRD of AlON (PDF card number: 01-080-2173) pellet pressureless sintered at 1950°C for 4 hours.

Samples were cut and polished to have a non-cuboidal shape. Pellets were cut into 3.5 mm cubes using a Chevalier FSSG-618 surface grinder fitted with a diamond cutting blade. To reduce the size further and spheroidize the samples, a Struers LaboPol-5 polishing equipment was used. Samples were manually polished on the wheel with a coarse 80 grit SiC grinding pad. This allowed for large removal of the edges and corners to produce noncuboidal samples with a size of approximately 3 mm.

3. ALUMINUM OXYNITRIDE MELTING

Levitated AlON samples were melted with a 400 W maximum continuous wave CO_2 (CW CO_2) laser at atmospheric pressure and 10.3 MPa in an ultra-high purity N_2 atmosphere and at atmospheric pressure in air to assess the effect of gas atmosphere and pressure on the chemistry of the samples. At atmospheric pressure, a volumetric flow rate of 1.20 SLM was supplied for levitation and an output power of 185 W was used to achieve melting, while at 10.3 MPa, a volumetric flow rate of 4.50 SLM was supplied, and an output power of 200 W was necessary for melting. An image from the melting process of these specimens is shown in Figure 3. As samples were not perfectly spherical, stable levitation was not able to be achieved, leading to samples not being fully melted. As seen in Figure 4, regions of the spheres melted at atmospheric pressure and 10.3 MPa did not melt, as indicated by the remaining non-spherical shape of the sample. This was similarly observed at atmospheric pressure in air. An attempt to achieve full melting was made by completing two runs with the sample being flipped between each run, allowing laser access to the “top” and “bottom” of the sample.

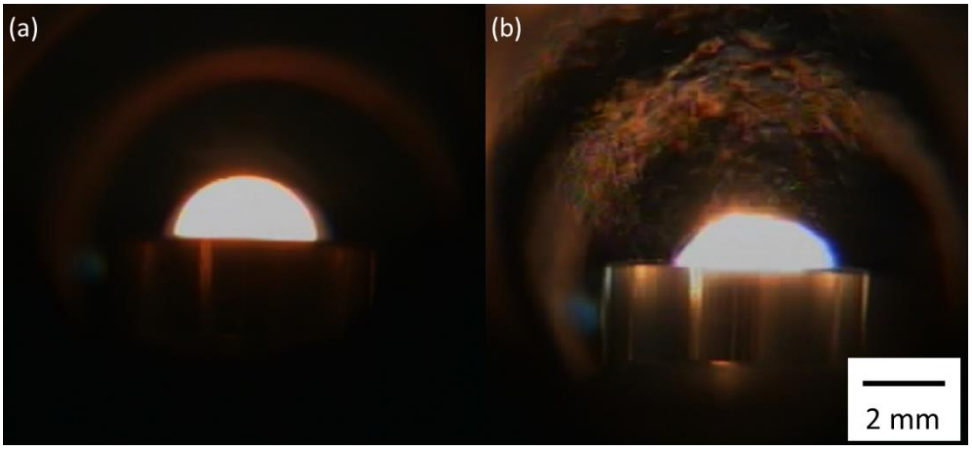

Figure 3: Specimens melting in N_2 at (a) atmospheric pressure and (b) 10.3 MPa.

Figure 4: Specimens melted in N_2 at atmospheric pressure (left) and at 10.3 MPa (right) with melted regions visible by the dome structure and unmelted regions noted by non-spherical shapes.

Upon melting the sample in N_2 at atmospheric pressure, some smoking from the sample and a total mass loss of 5.68 wt.% was observed. Two samples were melted at 10.3 MPa: one sample melted once and one sample melted in two separate runs on both the “top” and “bottom”. Upon melting, no smoking was observed from these samples, and a dome was formed on sides in contact with the laser. The sample melted once

showed no measurable mass loss, and instead a small mass gain of 0.06 wt.% was recorded. Similarly, the sample melted twice showed a total mass loss of 0.27 wt.%. These mass changes are summarized in Table 1.

Table 1: Mass change of samples melted in changing pressure conditions and gas mediums.

		Mass Change (wt.%)	
Pressure	**Gas Medium**	**First Melt Trial**	**Second Melt Trial**
Atmospheric	N_2	-2.87	-5.68
Atmospheric	Air	---	-3.82
10.3 MPa	N_2	---	+0.06
10.3 MPa	N_2	+0.06	-0.27

To compare the effect of the gas environment, a sample was melted in air at atmospheric pressure. This sample, prior to reaching the molten state, at an approximate apparent temperature of 1600°C, shattered, expanded, and oxidized to form Al_2O_3. The recovered sample can be seen in Figure 5, showing unreacted material with the initial grey coloring and Al_2O_3, as indicated by the white phase. As shown in Table 1, a mass loss of 3.82 wt.% was observed. However, not all material losses could be accounted for with this sample.

X-ray diffraction (XRD) was performed to attain a qualitative comparison of unmelted specimens and specimens melted at atmospheric pressure and 10.3 MPa. Figure 6a shows the XRD pattern for the “top” of the specimen melted in N_2 at an atmospheric pressure, while Figure 6b shows the XRD pattern for the “top” of the specimen melted in N_2 at 10.3 MPa. The collimated X-ray beam was aimed on the “top” of the specimens, in the melted zone. A 2 mm mask was used in an attempt to have a beam size on par with

the size of the specimen. However, due to the spherical shape of the specimens and the texture of these samples, the phases identified were considered qualitative and noise is present.

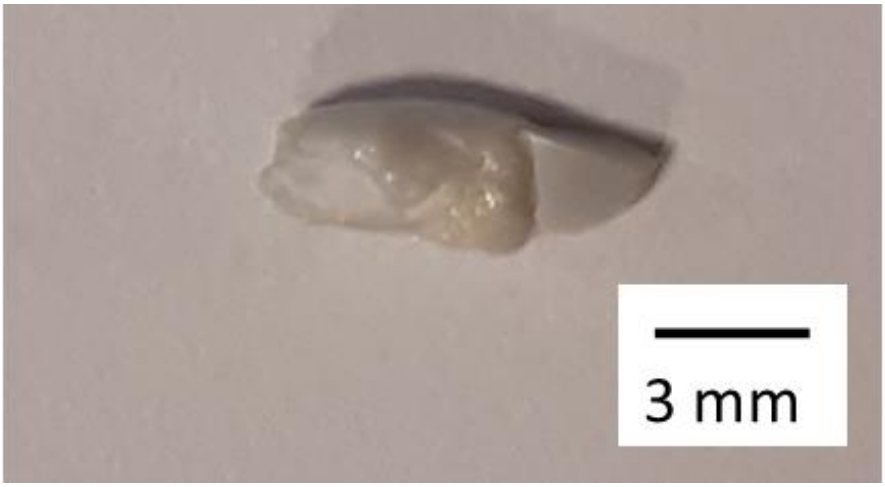

Figure 5: Sample processed in air at atmospheric pressure showing the formation of Al_2O_3 with remaining unoxidized AlON.

Nevertheless, the difference in the phase composition of the two samples processed at different conditions was discernable. At 10.3 MPa, the specimen appeared to be single phase AlON; however, at atmospheric pressure, there appeared to be the presence of another phase, tentatively identified as AlN, possibly due to Al_2O losses. The initial qualitative analysis indicated that increased N_2 pressure was necessary to retain the pure AlON phase, and decomposition occurred at atmospheric pressure. Further characterization is necessary to determine the decomposition pathway. XRD can additionally be used to determine the lattice parameter, which is affected by the nitrogen content and the overall N_2 pressure. However, this could not be attained using available laboratory XRD without destructive sample preparation.

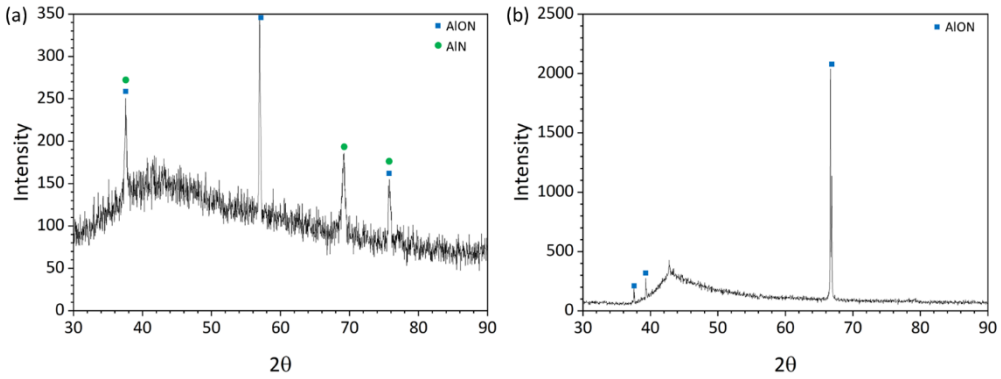

Figure 6: XRD with identified peaks of AlON specimens melted at (a) atmospheric pressure and (b) 10.3 MPa.

Additional XRD data is necessary to understand phase composition. Performing measurements with a synchrotron beamline would allow for more precise data that would allow for further information on phase preservation and lattice parameters to be gathered. The different processing environments are likely to cause a lattice parameter shift, as pressure and nitrogen content have been shown to affect lattice parameter. A gradient in composition can also be expected across the sample. Different phases and lattice parameters might be observed when comparing the umelted region, the region melted once, and the region melted twice.

Additional characterization to be completed includes X-ray photoelectron spectroscopy (XPS) to obtain information on the chemical state, electronic structure, and bonding. LECO oxygen/nitrogen analysis can be utilized to determine the oxygen and nitrogen content of the samples. Cross sections of the samples can be prepared for scanning electron microscopy (SEM) to view the materials' microstructure and Energy Dispersive Spectroscopy (EDS) for elemental composition information. This is scheduled to be conducted March 2023.

4. CONCLUSION

AlON specimens were melted in a hyperbaric aerodynamic levitator at varying conditions to determine the effect of gas medium and N_2 gas pressure on the phase composition of levitated samples. The sample melted in N_2 at atmospheric pressure noted a total mass loss of 5.68 wt.% after two runs, while the specimen melted in a N_2 gas atmosphere with a pressure of 10.3 MPa experienced a total mass loss of 0.27 wt.%. XRD phase compositions identified were qualitative and inconclusive; however, it can be noted that the two samples showed a difference in phase composition after melting. The specimen processed in air at atmospheric pressure oxidized and did not reach the melting point, exhibiting a mass loss of 3.82 wt.%. Further characterization is recommended with a synchrotron beamline. These results will provide quantitative XRD measurements to determine phases present and lattice parameters. Other characterization techniques, including XPS, LECO oxygen/nitrogen analysis, and SEM can be performed to characterize these specimens. This ongoing work will be completed and submitted for publication in the spring of 2023.

REFERENCES

1. H. Holleck. J. Vac. Sci. Technol. A 4 2661 (1986).
2. J.E. Sundgren, H.T.G. Hentzell. J. Vac. Sci. Technol. A 4 2259 (1986).
3. I. Milosev, B. Navinsek, H.H. Strehblow. Scientific Series of the International Bureau. Vol 37 (1995).

4. L. Swadzba, A. Maciejny, B. Formanek, P. Liberski, P. Podolski, B. Mendala, H. Gabriel, A. Poznanska. Surf. Coat. Technol. 78 137 (1996).

5. P. Panjan, B. Navinsek, A. Cvelbar, A. Zalar, I. Milosev. Thin Solid Films. 282, 298 (1996).

6. R.H. Greaves. Chromium Steels. His Majesty's Stationery Office, (1935).

7. A.B. Kinzel, R. Franks. The Alloys of lron and Chromium. Vol. H-High-Chromium Alloys (1940).

8. K.L. Lanskaya. Heat-Resistant and Refractory Steels. 2nd ed. (1979).

9. K. Frisk. CALPHAD. Vol. 15 No. 1, 79 (1991).

10. C.W. Bale, E. Bélisle, P. Chartrand, S.A. Decterov, G. Eriksson, A.E. Gheribi, K. Hack, I.H. Jung, Y.B. Kang, J. Melançon, A.D. Pelton, S. Petersen, C. Robelin. J. Sangster, P. Spencer and M.A. Van Ende. CALPHAD. Vol. 54, 35 (2016).

III. THE MELTING OF CHROMIUM NITRIDE IN A HYPERBARIC AERODYNAMIC LEVITATOR

1. INTRODUCTION

Within the chromium-nitrogen system, two nitrides are present: CrN (cubic) and Cr_2N (hcp). Chromium nitrides are important materials used frequently as coatings to protect against wear and corrosion.[1-3] Additionally, chromium nitrides provide hot corrosion resistance.[4,5] Chromium is used as an alloying element and chromium nitride formation is beneficial in steels to increase hardness and toughness.[6-8] Nitrides are of great interest; however, processing of chromium nitride can be challenging due to the decomposition of the material.

As an important high temperature material, understanding the behavior of chromium nitride at elevated temperatures is of interest. According to the phase diagram, Cr_2N has a melting point of approximately 1750°C at a N_2 pressure of 10 atm (1 MPa).[9] However, at atmospheric pressures, Cr_2N will decompose at temperatures of 1550°C to metallic Cr with total loss of nitrogen content. In order to avoid decomposition of this phase, an increased N_2 pressure is necessary.

$$2Cr_2N \rightleftharpoons 4Cr + N_{2\,(g)} \qquad \Delta G^o_{rxn} = -35.343kJ \; at \; T = 1750°C \tag{1}$$

To study the effect of N_2 pressure on the decomposition behavior of Cr_2N, a hyperbaric aerodynamic levitator was utilized to process samples at atmospheric and elevated pressure. The goal of this study was to demonstrate the benefits of containerless melt processing under high N_2 pressure for Cr_2N. This was completed by selecting a target specimen temperature in the liquid phase field and melting at atmospheric N_2

pressure and 5.52 MPa (800 psi), a pressure exceeding the decomposition pressure at 1750°C. After melting, samples were recovered for ex-situ phase and elemental analysis to determine whether the elevated pressure preserved the phase composition.

2. MATERIALS PREPARATION

To produce dense phase pure chromium nitride samples for levitation studies, a commercial CrN and Cr_2N powder mixture (Alfa Aesar) was hot-pressed. The as-received powder as shown in Figure 1a had an initial phase composition of metallic chromium (Cr) and a two-phase chromium nitride mixture, CrN and Cr_2N. Powder was loaded and compacted into a 25 mm graphite die before being hot pressed at 1300°C for 1 hour at 30 MPa with a heating and cooling rate of 20°C/min in a flowing N_2 atmosphere. The X-ray diffraction (XRD) results shown in Figure 1b of the hot-pressed billet demonstrate the material is phase pure upon equilibration.

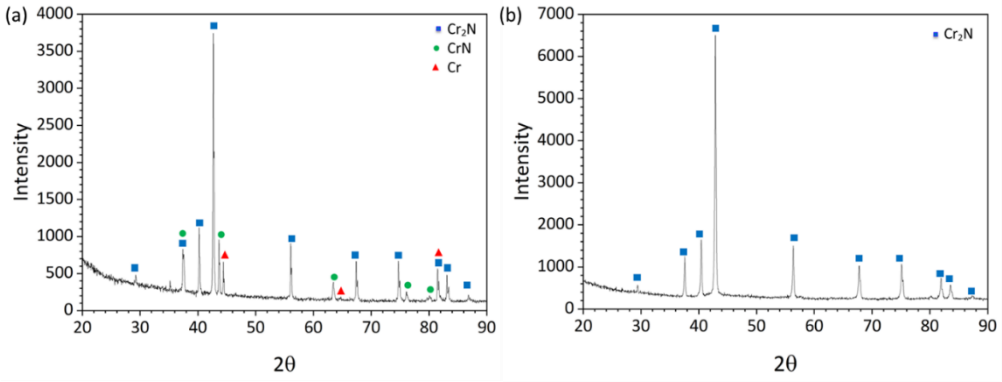

Figure 1: XRD identifying Cr (PDF card number: 00-006-0694), CrN (reference code: 01-076-2494), and Cr_2N (PDF card number: 00-035-0803) for (a) initial commercial CrN-Cr_2N powder mixture and (b) billet after hot pressing at 1300°C for 1 hour with 30 MPa.

Similar to the AlON sample processed in the previous section, these samples were required to be spherical or non-cuboidal for aerodynamic levitation. Pellets were cut into 3.5 mm cubes using a Chevalier FSG-618 surface grinder fitted with a diamond cutting blade. To reduce the size further and spheroidize the samples, a Struers LaboPol-5 polishing equipment was used. Samples were manually polished on the wheel with a coarse 80 grit SiC grinding pad. This allowed for large removal of the edges and corners to produce noncuboidal samples with a size of approximately 3 mm.

3. CHROMIUM NITRIDE MELTING

Cr_2N samples were melted with a 400W maximum CW CO_2 laser in the hyperbaric aerodynamic levitator in an ultra-high purity N_2 environment at both atmospheric pressure and an elevated pressure of 5.52 MPa. As Cr_2N is sensitive to oxygen due to Cr_2O_3 being very stable, an oxygen getter was installed to remove any residual O_2. This allowed for the gas stream to get down to 100PPT O_2, but limited the maximum pressure that could be achieved. At atmospheric pressure, 1.2 SLM was supplied for levitation and an output power of 200 W was necessary for melting, while at 5.52 MPa, 5.0 SLM was supplied for levitation and an output power of 260 W was required for melting. Due to the samples not being fully spherical, stable levitation was not achieved and melting was not uniform through the entirety of the sample. This nonuniform melting left a gradient on the samples, where the “top” (the point of laser contact) formed a dome from being molten and the “bottom” (the side not melted) remained slightly non-spherical.

The pyrometer read an apparent temperature in the range of 1400-1500°C while the specimen was molten. However, these values were associated with an emissivity value of 0.92, which is not standard for reflective metallic samples. This specimen appeared very similar to a metallic specimen due to the shiny, reflective surface. This metallic appearance made coupling with the laser more difficult, and emissivity corrected temperature could not be measured. The temperatures reached were likely higher than reported by the pyrometer due to its smaller emissivity value.

The sample melted at atmospheric pressure demonstrated a rapid volatilization once reaching the melting temperature. Figure 2 shows an image of the sample in the chamber after reaching the melting point. As shown in Figure 3, large amounts of material were lost, and the sample showed a total mass loss of 60.22 wt.%.

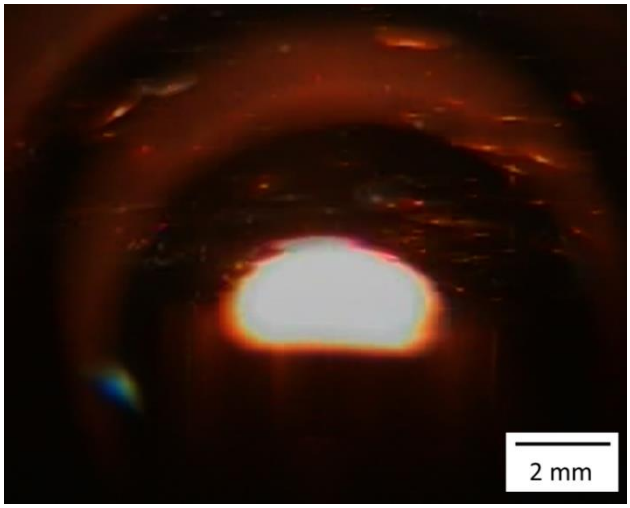

Figure 2: Melting of Cr_2N sphere at atmospheric pressure with spalling of material during heating.

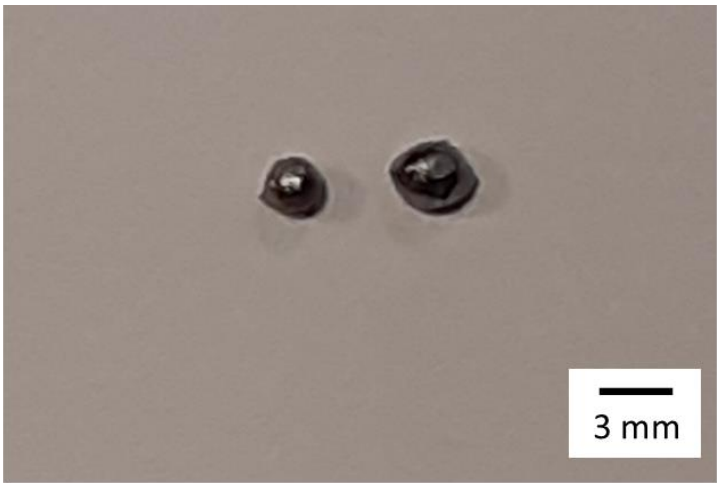

Figure 3: Specimens melted at atmospheric pressure (left) and 5.52 MPa (right) showing "top" melting regions and non-spherical unmelted regions.

When considering that the temperature was likely higher than the recorded pyrometer value, this 60.22 wt.% mass loss could correspond with the decomposition of Cr_2N as the mass change from Cr_2N to Cr metal was expected to be 11.86 wt.%. The observed value was in excess of the expected decomposition mass change, so additional material was lost via other mechanisms (e.g., Cr volatilization) as seen in Figure 2.

In comparison, the specimen melted at 5.52 MPa showed a significantly smaller total mass loss of 23.64 wt.%, and as visually seen in Figure 3, the material size did not see significant decrease when compared to the sample melted at atmospheric pressure. The increased fluid density of the N_2 demonstrated the capability of suppressing volatilization. However, this mass loss was in excess of the decomposition of Cr_2N, indicating that additional material was lost by another mechanism. This mass loss occurred over a longer exposure time when compared to the sample processed at atmospheric pressure. Initially, the chamber was pressurized to 5.52 MPa; however, the laser did not properly couple with the specimen and a molten state was not achieved. To

achieve this molten state, the pressure of the system was lowered to 1.38 MPa to reduce the convective heat transfer losses. The specimen was successfully melted at this condition, evident by a dome forming on the top of the specimen where the laser came into contact. The laser was then refocused and a successful attempt was made to achieve a molten state at 5.52 MPa.

To understand the decomposition of Cr_2N at atmospheric pressure and the effect of elevated nitrogen pressure, FactSage was utilized to construct phase diagrams at atmospheric pressure (1 atm) and 5.52 MPa (54 atm) as shown in Figure 4.[10] This was calculated using the Spencer Group database for carbide, boride, nitride, and silicide systems (SMCBN). As confirmed by these diagrams, Cr_2N does not achieve congruent melting at atmospheric pressure; however, it is achieved at 5.52 MPa. The Cr_2N phase extended as the N_2 pressure increased. At a temperature of 1800°C (estimated to be near the actual achieved temperature), the nitrogen content for the liquid was decreased to 16.2 mol% at atmospheric pressure when compared to the nitrogen content of 32.3 mol% at elevated pressure of 5.52 MPa.

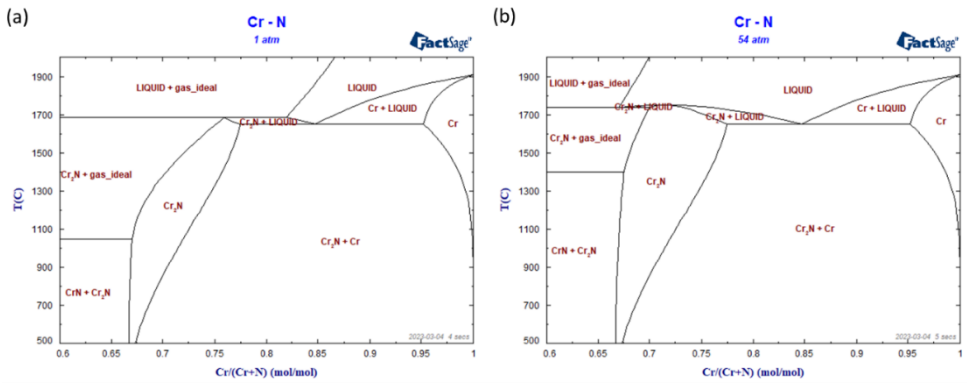

Figure 4: Phase diagrams of the Cr-N system constructed with FactSage (SMCBN) at (a) atmospheric pressure (1 atm) and (b) 5.52 MPa (54 atm).

XRD was performed on the melted “top” surface of both specimens to compare the phase composition. A 2 mm mask was used to reduce the beam size. However, the spherical shape and size of the specimens interfered with XRD measurements, providing only a qualitative comparison between the specimens. Figure 5 shows the phase compositions from XRD, which were determined to be inconclusive due to the sample shape and size and large beam size. On Figure 5a, the Cr_2N sample melted at atmospheric pressure showed a peak at 67.5° that lines up with Cr_2N. However, an accurate determination of the phase composition was difficult to achieve due to the large beam size and the inhomogeneity of the sample. No other peaks were discernable on this plot. Similarly, Figure 5b showed no clear phase composition identified. To attain clear phase composition, samples are planned to be analyzed with a synchrotron beamline. This would provide a more accurate assessment of the phases present to better understand the phase preservation at elevated pressures and compare it to the decomposition that occurred at atmospheric pressure.

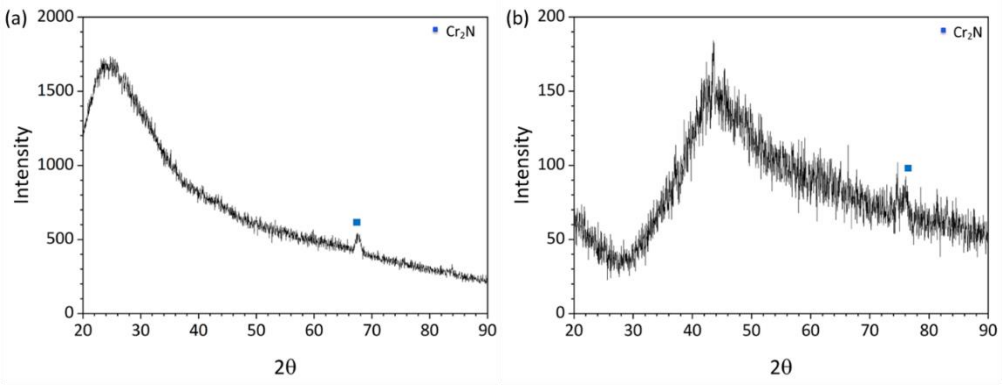

Figure 5: XRD of melt surface of Cr_2N sphere at (a) atmospheric pressure and (b) 5.52 MPa.

Additional characterization to be completed includes LECO oxygen/nitrogen analysis to determine the oxygen and nitrogen content of the samples. Cross sections of the samples will be prepared for scanning electron microscopy (SEM) to view the materials' microstructure, and Energy Dispersive Spectroscopy (EDS) can provide elemental analysis. This is scheduled to be conducted March 2023.

4. CONCLUSION

A hyperbaric aerodynamic levitator was used to melt Cr_2N at atmospheric pressure and an elevated pressure of 5.52 MPa to compare the effect of surpassing the decomposition pressure on the phase preservation. At atmospheric pressure, the specimen was expected to exhibit phase decomposition and a net loss of nitrogen content. This specimen demonstrated a significant weight loss of 60.22 wt.%; however, phase compositions identified with XRD were inconclusive due to the textured sample, as well as specimen shape and size. In contrast, the sample processed at a pressure above the decomposition pressure was expected to preserve the initial phase composition. This specimen had a smaller weight loss of 23.64 wt.%, and the XRD results were not able to conclusively show the phase present. Additional characterization, including XRD with a synchrotron beamline, is recommended for more conclusive results. This ongoing work will be completed and submitted for publication in the spring of 2023.

REFERENCES

1. S.A.T. Redfern, R.J Harrison, H.S.C O'Neill, D.R.R. Wood. Am. Mineralogist. 84, 299 (1999).

2. J.W. McCauley, N.D. Corbin. Nitrogen Ceramics. ed. F. L Riley, Martinus Nijhoff Pub., 111 (1983).

3. K. Zheng, H. Wang, P. Xu, H. Gu, B. Tu, W. Wang, S. Liu, Z. Fu. J. Eur. Ceram. Soc. 41, 4319 (2021).

4. I.G. Crouch, G.V. Franks, C. Tallon, S. Thomas, M. Naebe. Glasses and Ceramics. 7, 331 (2017).

5. J.W. McCauley, P. Patel, M. Chen, G. Gilde, E. Strassburger, B. Paliwal, K.T. Ramesh, D.P. Dandekar. J. Eur. Ceramic Soc. 29, 223 (2008).

6. N.D. Corbin. Thesis. M.S., Massachusetts Institute of Technology (1982).

SECTION

3. CONCLUSION

The research presented in this thesis focused on the development, testing, and use of a hyperbaric aerodynamic levitator. Hyperbaric aerodynamic levitation offers two main benefits in materials containerless processing research: suppression of volatile losses and the access of new chemical stability regions not achievable at atmospheric pressure conditions. The levitator was designed to operate at temperatures greater than 2000°C and pressures ranging from atmospheric to 10.3 MPa.

The levitation behavior was studied with varying sample size, sample density, pressure, and flow rate. Specimens of differing sizes and densities were systematically levitated with varying flow rates from 0-5.0 SLM and pressures ranging from atmospheric to 10.3 MPa. Levitation behavior was characterized by the vertical displacement of the specimen with increasing flow rate at a given pressure and stable levitation regimes were determined. As the volumetric flow rate increased at a given pressure, the vertical displacement increased for specimens of varying size and density. Additionally, as the pressure increased, the vertical displacement decreased for specimens of varying size and density. To understand the trends observed, the drag force was calculated for the changing experimental conditions. For lightweight specimens with diameters ranging from 2.5-3.5 mm, two stable levitation regimes were noted with increased pressure. This suggested that a change in drag force occurred with an increasing flow rate with a magnitude sufficient to displace the stable levitation position.

A change in the turbulent wake structure was speculated to be associated with the two observed stable levitation regimes for the lightweight specimens.

The convective heat transfer behavior of a levitated molten 3.0 mm diameter Al_2O_3 specimen was studied upon heating and cooling. The Al_2O_3 specimen was melted with a CW CO_2 laser to temperatures greater than 2000°C at a range of N_2 pressures from atmospheric to 10.3 MPa. The apparent temperatures of the specimens were recorded by optical pyrometry, and these values were used to create cooling curves of the levitated Al_2O_3 liquids as a function of N_2 pressure. The convective heat transfer coefficients were calculated from these cooling curves by fitting a convection-radiation heat equation. The convective heat transfer coefficient was shown to increase threefold as the pressure increased from atmospheric pressure to 10.3 MPa.

Along with determining the convective heat losses due to the increased fluid density, additional output laser power was necessary to melt specimens at elevated pressures. The necessary output laser power was compared at atmospheric pressure and 10.3 MPa, and it was determined that approximately 60 W additional laser power was required to melt the Al_2O_3 specimen at 10.3 MPa. As this increase is modest compared to the total output laser power available, it was determined that materials with greater melting temperatures could be melted using the hyperbaric aerodynamic levitator at elevated pressures. This study demonstrated that hyperbaric aerodynamic levitation is a promising technique for materials containerless processing research.

With the proven capability of a hyperbaric aerodynamic levitator, two materials were studied with this system: AlON and Cr_2N. AlON pellets of 35.7 mol% AlN were sintered, cut, and polished into specimens for levitation in the hyperbaric aerodynamic

levitator. These samples were melted with a CW CO_2 laser at atmospheric pressure and 10.3 MPa in an ultra-high purity N_2 gas, as well as at atmospheric pressure in air. Specimens did not achieve a fully molten state in any trial, despite repeating some trials with the sample flipped to melt the "top" and "bottom". At atmospheric pressure after two runs, a total mass loss of 5.68 wt.% was noted, while at 10.3 MPa after two runs, a total mass loss of 0.27 wt.% was observed. In air, the specimen did not reach the molten state and instead oxidized to form Al_2O_3. A mass loss of 3.82 wt.% was observed for the specimen levitated in air.

A qualitative XRD was performed on the "top" of the specimen melted twice at atmospheric pressure and 10.3 MPa. These initial results were not clear due to the sample size and shape as well as the texture of the sample. However, initial results indicated there were two phases present in the specimen melted at atmospheric pressure, while only the AlON phase was identified in the specimen melted at 10.3 MPa. N_2 pressure was expected to influence the lattice parameter and cause a shift due to the changing nitrogen content. The lattice parameter was expected to decrease with the increasing pressure due to the reduced nitrogen content from the suppression of Al_2O vapor. However, the lattice parameter was not able to be calculated due to the unclear phase identification; however, work with a synchrotron beamline could provide these results.

Additionally, Cr_2N specimens were sintered and processed for study with the hyperbaric aerodynamic levitator to determine the effect of N_2 pressure on decomposition and phase formation. Specimens were melted with a CW CO_2 laser at atmospheric pressure and 5.52 MPa in N_2 gas. At atmospheric pressure, Cr_2N will decompose at temperatures of 1550°C and assume a net loss of nitrogen content. To avoid

decomposition of the phases, an increased N_2 pressure is necessary, as Cr_2N has a melting point of approximately 1750°C when reaching a pressure of 1 MPa. When melted at atmospheric pressure, the Cr_2N specimen experienced a mass loss of 60.22 wt.% and spalling of material was observed once the molten state was achieved. In contrast, at 5.52 MPa, no visual loss of the sample mass was observed, and the mass loss was 23.64 wt.%. This supported the theory that increased pressure will suppress volatilization, and elevated pressure was necessary to maintain the initial phase. XRD of the two Cr_2N specimens was inconclusive due to the sample size, shape, and texture. However, initial phase composition identification showed that Cr_2N was still present after processing at both atmospheric pressure and 5.52 MPa. To improve the quality of XRD results, samples can be analyzed with a synchrotron beamline.

4. FUTURE WORK

This research has demonstrated the feasibility of a hyperbaric aerodynamic levitator for materials containerless processing. However, further improvements can be made to the system to allow for future studies of materials. For example, a new chamber design could allow for improved optical pyrometry, as the current design only has two 90° access windows.

The conical nozzle used for aerodynamic levitation can be designed to have different flow patterns. The converging-diverging nozzle cone semi-angle can vary from 30-60° and the orifice diameter can change as well. A future study could be completed to determine the optimal nozzle design for this system and assess whether different nozzles are best suited in different pressure regimes. Flow simulations and tests with a series of nozzles could be performed to understand the optimal design for stable levitation. Computational fluid dynamics (CFD) could be performed to study the effects of nozzle design on the levitation height achieved and levitation stability.

Additionally, further characterization for the two materials presented in this thesis, AlON and Cr_2N, would provide more conclusive results on the phases present and lattice parameters. Preliminary XRD has provided some qualitative information on the phase composition, but further information is necessary to fully characterize the effect of increased N_2 pressure. A synchrotron beamline can be used to provide XRD results for the materials melted at varying pressure conditions. This can also further provide lattice parameters for the AlON samples to understand if shifts occurred due to the increased N_2 pressure. Additional characterization to be performed includes XPS to gain bonding and

chemical information, LECO oxygen/nitrogen analysis, and SEM for microstructure imaging.

Completing improvements to the current system and understanding the results from the current nitride studies opens the possibility of future studies with a variety of materials. Future experiments can be completed by melting other materials that have a pressure dependence on decomposition or phase formation, including further work into high temperature nitrides. This hyperbaric aerodynamic levitator has a large impact on the future of materials research by allowing for the study of materials that are limited at atmospheric pressures. Phases that decompose at high temperatures and atmospheric pressures can be studied and measurements can be performed. This work can allow for the formation of novel phases and materials and provide a deeper understanding of the behavior and properties of molten materials under hyperbaric conditions.

BIBLIOGRAPHY

1. R. Weber, S.K. Wilke, C.J. Benmore. J. Phys. Soc. Jpn. 91, 091008 (2022).

2. E.C. Okress, D.M. Wroughton, G. Comenetz, P.H. Brace, J.C.R. Kelly. J. Appl. Phys. 23, 545 (1952).

3. G.R. Davies. Metall. Rev. 10, 173 (1965).

4. W.K. Rhim, S.K. Chung, D. Barber, K.F. Man, G. Gutt, A. Rulison, R.E. Spjut. Rev. Sci. Instrum. 64, 2961 (1993).

5. D.M. Herlach, R.F. Cochrane, I. Egry, H.J. Fecht, A.L. Greer. Int. Mater. Rev. 38, 273 (1993).

6. G. Jacobs, I. Egry, K. Maier, D. Platzek, J. Reske, R. Frahm. Rev. Sci. Instrum. 67, 3683 (1996).

7. C. Landron, X. Launay, J.C. Rifflet, P. Echegut, Y. Auger, D. Riffier, J.P. Coutures, M. Lemonier, M. Gailhanou, M. Bessiere, D. Bazin, H. Dexpert. Nucl. Instrum. and Methods in Phys. Res. B124, 627 (1997).

8. S. Krishnan, J.J. Felten, J.E. Rix, J.K.R. Weber, P.C. Nordine, M.A. Beno, S. Ansell, D.L. Price. Rev. Sci. Instrum. 68, 3512 (1997).

9. P.F. Paradis, T. Ishikawa, J. Yu, S. Yoda. Rev. Sci. Instrum. 72, 2811 (2001).

10. L. Hennet, D. Thiaudière, M. Gailhanou, C. Landron, J.P. Coutures, D.L. Price. Rev. Sci. Instrum. 73, 124 (2002).

11. L. Hennet, I. Pozdnyakova, A. Bytchkov, V. Cristiglio, P. Palleau, H.E. Fischer, G.J. Cuelle, M. Johnson, P. Melin, D. Zanghi, S. Brassamin, J.F. Brun, D.L. Price. Rev. Sci. Instrum. 77, 053903 (2006).

12. J.K.R. Weber, A. Tamalonis, C.J. Benmore, O.L.G. Alderman, S. Sendelbach, A. Hebden, M.A. Williamson. Rev. Sci. Instrum. 87, 073902 (2016).

13. J.K.R. Weber. Int. J. Appl. Glass Sci. 1, 248 (2010).

14. J.K.R. Weber, D.S. Hampton, D.R. Merkley, C.A. Rey, M.M. Zatarski, P.C. Nordine. Rev. Sci. Instrum. 65, 456 (1994).

15. M. Chesswas, B. Cockayne, D.T.J. Hurle, E. Jakeman, J.B. Mullin. J. Cryst. Growth. 11, 225 (1971).

16. J.S. Haggerty, J.L. O'Brien, J.F. Wenckus. J. Crystal Growth 3/4, 291 (1968).

17. L.C.F. Blackman, P.H. Dundas, A.W. Moore, A.R. Ubbelohde. Brit. J. Appl. Phys. 12, 377 (1961).

18. H. Van Hook, Rev. Sci. Instrum. 36, 1119 (1965).

19. A.R. Bradshaw, D. Fort. Rev. Sci. Instrum. 63, 5459 (1992).

20. C. Ronchi, J.P. Hiernaut, R. Selfslag, G.J. Hyland. Nucl. Sci. Eng. 113, 1 (1993).

21. S. Möhr, H. Müller-Buschbaum. Angew. Chem. Int. Ed. Engl. 34, 634 (1995).

22. S. Hosokawa, W.C. Pilgrim. Rev. Sci. Instrum. 72, 1721 (2001).

23. D. Manara, C. Ronchi, M. Sheindlin. Int. J. Thermophys. 23, 1147 (2002).

24. D. Manara, M. Sheindlin, W. Heinz, C. Ronchi. Rev. Sci. Instrum. 79, 113901 (2008).

25. F. De Bruycker, K. Boboridis, R.J.M. Konings, M. Rini, R. Eloirdi, C. Guéneau, N. Dupin, D. Manara. J. Nucl. Mater. 419, 186 (2011).

26. J.L. Schmehr, M. Aling, E. Zoghlin, S.D. Wilson. Rev. Sci. Instrum. 90, 043906 (2019).

27. J.W. McCauley, P. Patel, M. Chen, G. Gilde, E. Strassburger, B. Paliwal, K.T. Ramesh, D.P. Dandekar. J. Eur. Ceram. Soc. 29, 223 (2008).

28. K. Zheng, H. Wang, P. Xu, H. Gu, B. Tu, W. Wang, S. Liu, Z. Fu. J. Eur. Ceram. Soc. 41, 4319 (2021).

29. K. Frisk. CALPHAD. Vol. 15 No. 1, 79 (1991).

30. H. Holleck. J. Vac. Sci. Technol. A 4, 2661 (1986).

31. J.E. Sundgren, H.T.G. Hentzell. J. Vac. Sci. Technol. A 4, 2259 (1986).

32. I. Milosev, B. Navinsek, H.H. Strehblow. Scientific Series of the International Bureau. Vol. 37, 108 (1995).

33. C.J. Benmore, J.K.R. Weber. Advances in Physics: X 2, 717 (2017).

34. R.J. Naumann. Historical Development (1986). In: B. Feuerbacher, B. Hamacher, R.J. Naumann, Materials Sciences in Space A Contribution to the Scientific Basis of Space Processing. 11 (1986).

35. D. Langstaff, M. Gunn, G.N. Greaves, A. Marsing, F. Kargl. Rev. Sci. Instrum. 84, 124901 (2013).

36. B. Glorieux, F. Millot, J.C. Rifflet, J.P. Coutures. Int. J. Thermophys. 20, 1085 (1999).

37. P.F. Paradis, T. Ishikawa, S. Yoda. Meas Sci Technol. 16, 94 (2005).

38. P.F. Paradis, J. Yu, T. Ishikawa, T. Aoyama, S. Yoda. Appl. Phys. A 79(8), 1965 (2004).

39. K. Ohsaka, S.K. Chung, W.K. Rhim. Acta Mater. 46, 4535 (1998).

40. S. Ushakov, A. Shvarev, T. Alexeev, D. Kapush, A. Navrotsky. J. Am. Ceram. Soc. 100, 754 (2016).

41. A. Navrotsky, S. Ushakov. Am. Ceram. Soc. Bull. 96(2) (2017).

42. Y. Arai, P.F. Paradis, T. Aoyama, T. Ishikawa, S. Yoda. Rev. Sci. Instrum. 74(2), 1057 (2003).

43. K. Bucks, H. Muller. Z. Phys. 84, 75 (1933).

44. E.H. Trinh. Rev. Sci. Instrum. 56, 2059 (1985).

45. S.E. Wolf, J. Leiterer, M. Kappl, F. Emmerling, W. Tremel. J. Am. Chem. Soc. 130, 12342 (2008).

46. J. Leiterer, W. Leitenberger, F. Emmerling, A.F. Thunemann, U. Panne. J. Appl. Cryst. 39, 771 (2006).

47. J.K.R. Weber, C.A. Rey, J. Neuefeind, C.J. Benmore. Rev. Sci. Instrum. 80, 083904 (2009).

48. C.J. Benmore, J.K.R. Weber, A.N. Tailor, B.R. Cherry, J.L. Yarger, Q. Mou, W. Weber, J. Neuefeind, S.R. Byrn. J. Pharm. Sci. 102, 1290 (2013).

49. M.A. Andrade, N. Perez, J.C. Adamowski, Braz. J. Phys. 48, 190 (2017).

50. M. Barmatz. MRS Proceedings. 9 (1982).

51. O. Muck. German Patent # 42204 (1923).

52. I. Egry, D. Holland-Moritz. Eur. Phys. J. Special Topics. 196, 131 (2011).

53. R.W. Hyers, J.R. Rogers. High Temperature Materials and Processes. Vol. 27(6), 461 (2008).

54. D.A. Winborne, P.C. Nordine, D.E. Rosner, N.F. Marley. Metall. Trans. B 7, 711 (1976).

55. J.P. Coutures, J.C. Rifflet, D. Billard, P. Coutures. Proc. 6th Eur. Symp. on Materials Sciences under Microgravity Conditions. Bordeaux, Dec. 2–5 (1986).

56. J.K.R. Weber, C.J. Benmore, L.B. Skinner, J. Neuefeind, S.K. Tumber, G. Jennings, L.J. Santodonato, D. Jin, J. Du, J.B. Parise. J. Non-cryst. Solids. 383, 49 (2014).

57. C.J. Benmore, M.C. Wilding, J.K.R. Weber. Eur. Phys. Lett. 89, 1 (2010).

58. C.J. Benmore, J.K.R. Weber, K.J. Hiera. Appl. Phys. Lett. 24, 4954 (2010).

59. S. Kohara, K. Suzuya, K. Takeuchi, C.-K. Loong, M. Grimsditch, J.K.R. Weber, J.A. Tangeman, T.S. Key. Science. 303, 1649 (2004).

60. "Aerodynamic levitation processing of a zr-based bulk metallic glass," Mater. Sci. and Eng.: A 445-446, 219 (2007).

61. Q. Mei, C.J. Benmore, J.E. Siewenie, J.K.R. Weber, M.C. Wilding. J. Phys.: Condens. Matter. 20, 245106 (2008).

62. J.K.R. Weber, S. Sen, R. Youngman, R. Hart, C. Benmore. J. Phys. Chem. B 112, 16726 (2008).

63. S. Sen, J. Tangeman. Am. Mineralogist. 93, 946 (2008).

64. S. Sen, H. Maekawa, G. Papatheodorou. J. Phys. Chem. B 113, 15243 (2009).

65. L. Skinner, A. Barnes, P. Salmon, W. Crichton. J. Phys.: Condens. Matter. 20, 205103 (2008).

66. D.L. Price. High Temperature Levitated Materials. Cambridge University Press, 2010.

67. C. Shi, O.L.G Alderman, A. Tamalonis, R. Weber, J. You, C.J. Benmore. Commun. Mater. 1, 80 (2020).

68. S.J. McCormack, A. Tamalonis, J.K.R. Weber, W.M. Kriven. Rev. Sci. Instrum. 90, 015109 (2019).

69. S. Krishnan, J.J. Felten, J.E. Rix, J.K.R. Weber, P.C. Nordine, M.A. Beno, S. Ansell, D.L. Price. Rev. Sci. Instrum. 68, 3512 (1997).

70. S.J. McCormack, R.J. Weber, W. M. Kriven. Acta Mater. 161, 127 (2018).

71. S.J. McCormack, K.P. Tseng, R. Weber, D. Kapush, S.V. Ushakov, A. Navrotsky, W.M. Kriven. J. Am. Ceram. Soc. 102(8), 4848 (2019).

72. C.J.E. Santos, A.Z. Nelson, E. Mendoza, R.H. Ewoldt, W.M. Kriven. J. Eur. Ceram. Soc. 35, 3587 (2015).

73. K.T. McDonald. Am. J. Phys. 68, 388 (2000).

74. W.A. Phelan, J. Zahn, Z. Kennedy, T.M. McQueen. J. Solid State Chem. 270, 705 (2019).

75. J. Zhang, H. Zheng, Y. Ren, J.F. Mitchell. Cryst. Growth Des. 17, 2730 (2017).

76. J.L. Schmehr, M. Aling, E. Zoghlin, S.D. Wilson. Rev. of Sci. Instrum. 90, 043906 (2019).

77. J. Zhang, H. Zheng, C.D. Malliakas, J.M. Allred, Y. Ren, Q. Li, T. Han, J.F. Mitchell. Chem. Mater. 26, 7172 (2014).

78. H.B. Cao, Z.Y. Zhao, M. Lee, E.S. Choi, M.A. McGuire, B.C. Sales, H.D. Zhou, J. Yan, D.G. Mandrus. APL Mater. 3, 062512 (2015).

79. Z.W. Li, C. Liu, M. Skoulatos, L.H. Tjeng, A.C. Komarek. J. Cryst. Growth. 427, 94 (2015).

80. H. Guo, Z. Hu, T. Pi, L.H. Tjeng, A.C. Komarek. Crystals. 6, 98 (2016).

81. J. Zhang, A.S. Botana, J.W. Freeland, D. Phelan, H. Zheng, V. Pardo, M.R. Norman, J.F. Mitchell. Nat. Phys. 13, 864 (2017).

82. C. Neef, H. Wadepohl, H. Meyer, R. Klingeler. J. Cryst. Growth. 462, 50 (2017).

83. N.J. Schreiber, J. Zhang, H. Zheng, J.W. Freeland, Y. Chen, J.F. Mitchell, D. Phelan. J. Solid State Chem. 254, 69 (2017).

84. H. Guo, Z.W. Li, L. Zhao, Z. Hu, C.F. Chang, C.Y. Kuo, W. Schmidt, A. Piovano, T.W. Pi, O. Sobolev, D.I. Khomskii, L.H. Tjeng, A.C. Komarek. Nat. Commun. 9, 43 (2018).

85. C.A. Rey, R. Sisler, D.R. Merkley, T.J. Danley. Prog. Astronaut. Aeronaut. 127, 270 (1990).

86. D. Borosa, S. Kareth, M. Petermann. Chem. Ing. Tech. 84, 145 (2012).

87. J. Magill, F. Capone, R. Beukers, P. Werner, R.W. Ohse. High Temp.-High Pressures. 19, 461 (1987).

88. R.W. Ohse. Int. J. Thermophys. 11, 753 (1990).

89. M.V. Kumar, J.T. Okada, T. Ishikawa, P.F. Paradis, Y. Watanabe. Meas. Sci. Technol. 25, 085301 (2014).

90. N.H. El-Kaddah, D.G.C. Robertson. Metall. Trans. B, 9B, 191 (1978).

91. Ts.V. Rashev, R.I. Ivanov, L. Saraiyanov. Zavod. Lab. 44, 550 (1978).

92. I.G. Crouch, G.V. Franks, C. Tallon, S. Thomas, M. Naebe. Glasses and Ceramics. 7, 331 (2017).

93. J.W. McCauley, N.D. Corbin, Nitrogen Ceramic. ed. F. L Riley, Martinus Nijhoff Pub. 111 (1983).

94. G. Yamaguchi, H. Yanagida. Bull. Chem. Soc. 32 Jpn. 1085(1959).

95. Y. W. Kim, B.H. Park, H.C. Park, Y.B. Lee, K.D. Oh, F. Riley. Br. Ceram. Trans. 97, 97 (1998).

96. Y. W. Kim, B.H. Park, H.C. Park, Y.B. Lee, K.D. Oh, R. Stevens. J. Eur. Ceram. Soc. 21, 2383 (2001).

97. A. Maghsoudipour, M.A. Bahrevar, J.G. Heinrich, F. Moztarzadeh. J. Eur. Ceram. Soc. 25, 1067 (2005).

98. W. Rafaniello, I. Cutler. J. Am. Ceram. Soc. 64, 533 (1981).

99. S. Balasubramanian, R.K. Sadangi, V. Shukula, B.H. Kear, D.E. Niesz. Ceram. Trans. 148, 83 (2004).

100. H. Fukuyama, W. Nakao, M. Susa, K. Nagata. J. Am. Ceram. Soc. 82, 1381 (1999).

101. D. Zientara, M.M. Bucko, J. Lis. J. Eur. Ceram. Soc. 27, 775 (2007).

102. T.G. Akopdzhanyan, S.I. Rupasov, S. Vorotilo. Combustion and Flame. 232, 111560 (2021).

103. N.D. Corbin. M.S. Thesis. Massachusetts Institute of Technology (1982).

104. L. Swadzba, A. Maciejny, B. Formanek, P. Liberski, P. Podolski, B. Mendala, H. Gabriel, A. Poznanska. Surf. Coat. Technol. 78, 137 (1996).

105. P. Panjan, B. Navinsek, A. Cvelbar, A. Zalar, I. Milosev. Thin Solid Films. 282, 298 (1996).

106. R.H. Greaves. Chromium Steels. His Majesty's Stationery Office, 275 (1935).

107. A.B. Kinzel, R. Franks. The Alloys of lron and Chromium. Vol. H-High-Chromium Alloys (1940).

108. K.L. Lanskaya. Heat-Resistant and Refractory Steels. 2nd ed. (1979).

109. C.L. Yeh, E.W. Liu. J. Alloys Compd. 426 (1–2), 131 (2006).

110. L.E. Toth. Transition Metal Carbides and Nitrides. Academic Press, New York, (1971).

111. K. Hirota, Y. Takano, M. Yoshinaka, O. Yamaguchi. J. Am. Ceram. Soc. Vol. 84, Issue 9, 2120 (2001).

VITA

Sydney Boland grew up in St. Louis, Missouri. Sydney attended high school in St. Louis and graduated in 2017 before moving to Rolla, Missouri to attend Missouri University of Science and Technology (Missouri S&T) that fall. She declared her major as Ceramic Engineering upon acceptance, and she was officially accepted into the department in the Fall of 2018. During her four years at Missouri S&T, Sydney was a member of the Concrete Canoe Design Team and Zeta Tau Alpha Fraternity. Beginning in the Fall of 2018, Sydney joined the KERAMOS chapter of Missouri S&T. She held multiple leadership positions on the Concrete Canoe Design Team, including STUCO Representative (FS18), Treasurer (FS19-SS20), and Chief Engineer (FS20-SS21), as well as performing as the Treasurer of the KERAMOS chapter (FS19-SS20) and Historian of the KERAMOS chapter (FS20-SS21). During her undergraduate career, Sydney worked for GE Aviation as a co-op and as an intern. Sydney received her B.S. degree in Ceramic Engineering from Missouri S&T in the Spring of 2021.

Sydney began her graduate work as a master's student for Dr. David W. Lipke at Missouri S&T in June of 2021. During her graduate career, Sydney focused her research on the development and testing of a hyperbaric aerodynamic levitation system. Sydney has published one paper on this topic and plans to submit two more. She graduated with a M.S. in Materials Science and Engineering in May 2023 from Missouri S&T.